Effect of Thermal Boundary Condition on the Convective Flow of Nano-Fluid Through a Cylinder



By:

Selah Ud Deen Ahmed Gulzar

Reg. No. 965-FBAS/MSMA/F23

Department of Mathematics and Statistics
Faculty of Sciences
International Islamic University, Islamabad
Pakistan
2025

Effect of Thermal Boundary Condition on the Convective Flow of Nano-Fluid Through a Cylinder



By:

Selah Ud Deen Ahmed Gulzar

Reg. No. 965-FBAS/MSMA/F23

Supervised By:

Dr. Rahmat Ellahi

Department of Mathematics and Statistics
Faculty of Sciences
International Islamic University, Islamabad
Pakistan
2025

Effect of Thermal Boundary Condition on the Convective Flow of Nano-Fluid Through a Cylinder

By:

Selah Ud Deen Ahmed Gulzar

Reg. No. 965-FBAS/MSMA/F23

A Thesis

Submitted in the Partial Fulfillment

of the Requirements for Degree of

MASTER OF SCIENCE

IN

MATHEMATICS

Supervised By:

Dr. Rahmat Ellahi

Department of Mathematics and Statistics
Faculty of Sciences
International Islamic University, Islamabad
Pakistan
2025

DEDICATION

I express my heartfelt gratitude and utmost respect as I dedicated this work to my beloved

Hazrat Muhammad (S.A.W),

and

My dear Parents

They have been a constant source of inspiration and encouragement, guiding me towards greater virtues in life.

DECLARATION

I hereby declare that the work presented in this thesis is my own effort, except where otherwise acknowledged, and that the thesis is my own composition. No part of the thesis has been previously presented for any other degree.

Date	<u> </u>		

Mr. Selah Ud Deen Ahmed Gulzar
MS in Mathematics
965-FBAS/MSMA/F23

ACKNOWLEDGEMENTS

In the name of Allah, the most gracious and the most merciful. First and foremost, I am

thankful to Almighty ALLAH for guiding me on the path of knowledge after creating

us as human beings and giving me the strength, knowledge, ability, and opportunity to

undertake this study and complete it satisfactorily. All the presses to our beloved

prophet Hazrat Muhammad (S.A.W) the source of kindness, humanity and whom

Allah send for the guidance of the whole world and who declared it an obligatory duty

of every Muslim to seek and procure knowledge. May Allah shower his countless

blessing upon **Muhammad** (SAW) and his family.

I would like to express my special appreciation and thanks to my teachers and

supervisor Professor Dr. Rahmat Ellahi and Professor Dr. Ahmad Zeeshan you

have been a tremendous mentor for me. I would like to thank you for the encouragement

and support you have shown towards my research. Your tireless work, unique way of

research and devotion to your profession cannot be expressed in words.

I am extremely grateful to my seniors Dr. Muhammad Imran and Dr. Amad Ur

Rehman for their support throughout this process. They guided me throughout my

research work and their encouragement, observation, attitude, and support of kindness

meant a lot. I thank my colleagues Mr. Naeem Bashir and Mr. Hameedullah khan

and other fellows and friends who deserve formal acknowledgement but could not be

named individually.

I am extremely grateful to My Parents and Siblings for their support, encouragement,

and genuine interest in my academic success. The selfless prayers and good wishes of

my parents have always been the source of my success in all aspects of my life. I am

thankful to My Father for his moral and financial support without that I could have not

pursued my dream.

Mr. Selah Ud Deen Ahmed Gulzar

965-FBAS/MSMA/F23

iii

Table of Contents

Chapte	r 1
Definiti	ons1
1.1	Fluid1
1.2	Fluid Mechanics
1.2.	1 Types of Fluid Mechanics
1.2.	2 Properties of Fluids2
1.2.	3 Fluid Flow: 3
1.2.	4 Types of Fluids4
1.3	Nanofluid5
1.4	Equation of Continuity6
1.5	Navier-Stokes Equation6
1.6	Bernoulli's Equation
1.7	Flow Measurement
1.8	COMSOL Multiphysics9
1.8.	1 Application of COMSOL Multiphysics in Fluid Mechanics:11
Chapte	r 212
	cal Investigation of Blood Flow on Hybrid Nanofluid with Heat Transfer a Curvy Stenotic Artery: Silver and Gold12
2.1	Introduction
2.2	Mathematical Modeling:
2.3	Results and Discussion

2.4	Conclusion	28
Chapte	er 3	30
	of Thermal Boundary Condition on the Convective Flow gh a Cylinder	
3.1	Introduction	30
3.2	Mathematical Modelling	31
3.3	Results and Discussion	38
3.4	Conclusion	62
Refere	nces	64

LIST OF FIGURES

Fig. 2. 1: Geometry of the artery	14
Fig. 2. 2: Inlet of the artery	15
Fig. 2. 3: Outlet of the artery	15
Fig. 2. 4: Walls of the stenotic artery	16
Fig. 2. 5: Insolated walls.	16
Fig. 2. 6: temperature 1	17
Fig. 2. 7: Temperature 2	17
Fig. 2. 8: Mesh of the artery	17
Fig. 2. 9: Surface velocity magnitude at different time intervals	18
Fig. 2. 10: Velocity profile in x-component at different times	19
Fig. 2. 11: Velocity profile in y-component at different times	20
Fig. 2. 12: Pressure contour at different times	21
Fig. 2. 13: Convective heat flux in x-axis at different times.	23
Fig. 2. 14: Heat flux at y-axis at different time intervals	24
Fig. 2. 15: Surface temperature at different time intervals	25
Fig. 2. 16: Temperature contours at different time intervals	26
Fig. 2. 17: Streamlines at different time intervals	27
Fig. 3. 1 Geometry of the single solid obstacle	32
Fig. 3. 2 Geometry of the double solid obstacles	32
Fig. 3. 3 Inlet	34
Fig. 3. 4 Outlet	35
Fig. 3. 5 Velocity at wall	35
Fig. 3. 6 Thermal insolation	36

Fig. 3. 7 Temperature 1	36
Fig. 3. 8 Temperature 2	37
Fig. 3. 9 Mesh	37
Fig. 3. 10 Velocity magnitude for single solid obstacle.	39
Fig. 3. 11 Velocity magnitude for double solid obstacles.	42
Fig. 3. 12 Velocity profile at x-axis for single solid obstacle	44
Fig. 3. 13 Velocity profile at y-axis for single solid obstacle	45
Fig. 3. 14 Velocity profile at x-axis for double solid obstacles	47
Fig. 3. 15 Velocity profile at y-axis for double solid obstacles	48
Fig. 3. 16 Pressure contour for single solid obstacle	52
Fig. 3. 17 Pressure contour for double solid obstacles	54
Fig. 3. 18 Surface temperature for single solid obstacle	56
Fig. 3. 19 Surface temperature for double solid obstacles	58
Fig. 3. 20 Lift coefficient, CL, as a function of time for single solid obstacle	59
Fig. 3. 21 Drag coefficient, CD, as a function of time for single solid obstacle	59
Fig. 3. 22 Lift coefficient, CL, as a function of time for double solid obstacles	60
Fig. 3. 23 Drag coefficient, CD, as a function of time for double solid cylinder	61

LIST OF TABLES

Table. 2. 1 Display the thermophysical characters of the base fluid and nanopartic		
	28	
Table. 2. 2 Mesh size and mesh properties	28	
Table. 3. 1 Mesh size and mesh properties for single solid cylinder	62	
Table. 3. 2 Mesh size and mesh properties for double solid cylinder	62	

PREFACE

Dispersed, engineered suspension nanostructures with sizes ranging from 1 to 100 nm make up nanofluids. Water, motor oil, biofluids, organic fluids, and other basic fluids are commonly referred to as base fluids. Common materials used as nanomaterials include metals, various carbon structures, and nanostructures. Numerous potential applications have been made possible by the use of nanofluid. Choi [1] was the first to investigate thermal performance improvements in nanofluids. Among the various types of nanofluids are heat exchangers, bio and pharmacological nanofluids, medical nanofluids, environmental nanofluids, and so on. The impact of fluid size, concentration, structure, and other variables on thermal efficiency was studied by many researchers. Narrowing arteries known as arterial stenoses can worsen over time, obstructing blood flow to organ systems and possibly resulting in death. In contrast to base fluids, the addition of solid micrometer atoms improves the fluid's thermal properties and heat transfer rates. As a result, scientists are now more interested in nanofluids because of their applications in industry, telecommunication, and medicine. Through an experimental investigation, Yan et al. [2] looked into the rheological behavior of nanoparticles. Elelamy et al. [3] investigated the blood flow of a nanofluid with temperature distribution and slip condition in a heart valve. Numerous recent studies [4-6] have examined the addition of nanomaterials while accounting for the base fluid. The impact of substrate concentration on blood flow through a stenosed artery has been extensively studied theoretically. Examples of arterial diseases that can drastically change the characteristics of blood flow in arteries are aneurysms and stenosis. Blood vessel stenosis is a very common condition that can result from lipid buildup within the vascular system. When a lesion spreads into the lumen of an artery, stenosis results. When stenosis develops in an artery of that type, one of the worst

consequences of this restriction is an increase in resistance and, as a result, a decrease in blood flow through the artery. Therefore, serious arterial and cardiovascular problems could result from the development of stenosis. Chahregh and Dinarvand [7] investigated blood-based nanofluid flow via an artery with medication administration and cardiovascular system in acute respiratory applicability. The effect of penetration on blood flow for nanofluids across bifurcated stenosed arteries was examined by Shahzadi and Bilal [8]. Abdelsalam et al. [9] described the alterations in blood flow brought on by the forces of nanofluid via such an artery segment. Basha et al. [10] used finite difference computation to study the bio-nanofluid flow in an intrinsically motivated artery. Several researchers have studied the effects of stenosis on flow characteristics both theoretically and practically, despite the fact that its exact cause is unknown [11–13]. Gold nanoparticles have proven to be useful tools in a variety of nanomedical applications because of their photo-optical characteristics. Biological systems are generally stable and inert. Furthermore, gold nanoparticles in trace amounts don't appear to be dangerous. Gold nanoparticles have potential uses in diagnostics, health, and physiological therapy. The use of gold nanoparticles in the management of vascular disorders is still being investigated. A clinical study involving 180 participants found that the amount of plaque was decreased by plasmatic UV thermal treatment and gold infusion through an on-artery patch. There are currently no mathematical equations that have been used to study the blood flow of metallic nanoparticles via stenosed arteries. Bhatti [14] examined the physiologically inspired intrauterine nanofluid flow that occurs when magnetic gold There are uses for nanopowders in biomedicine. Bhatti [14] looked into the physiologically inspired intrauterine nanofluid flow that occurs when magnetic gold There are uses for nanopowders in biomedicine. The impact of the form factor on the hybrid nanofluid containing nanoparticles was

illustrated by Waqas et al. [15]. Blood flow in a stenosed, narrowed tube with different viscosities of nanofluids:

Elnaqueb et al. [16] discuss the hemodynamic characteristics of gold nanoparticles. Khan et al. [17] investigated the effect of a magnetic field on Sisko fluid flow with metallic nanoparticles over a porous curved surface with partial slip and radioactivity. An integral component of the circulatory system are blood vessels. The primary function of the circulatory system is to eliminate waste products and deliver oxygen and other nutrients to active tissues. Nowadays, gold nanoparticles are frequently studied and used in bioengineering and biomedicine. Gold nanoparticles are increasingly being used in lab-on-a-chip research in the areas of biology, drug delivery, cancer treatment, immunological modulation, implants, and prosthetics. COMSOL Multiphysics is a powerful simulation program used in many areas of physics, engineering, and research. Solving coupled systems of PDEs in challenging multiphysics problems is its primary responsibility, simulates the possible static and dynamic behavior of electrical systems. investigates the connection between the mechanical, thermal, and electromagnetic properties of a material. used in classrooms to teach pupils challenging arithmetic, engineering, and physics concepts. COMSOL Multiphysics allows users to build models that include a range of physical phenomena and their interactions by combining these multiple applications into a single platform. Its versatility makes it an invaluable tool for conducting cutting-edge scientific research and addressing practical engineering problems. Salvi et al. [18] investigated the accuracy of the thermodynamic values predicted for the CMC outcome (R2 = 0.9) and tap water (R2 = 0.85), even though they used a coarser mesh size because of storage limitations. Sezgin et al. [19] looked into simulating an extreme temperature PEM fuel cell using COMSOL Multiphysics. One flow channel is thought to exist in the model.

The experiment is conducted using the Fuel Cells & Batteries Modules of licensed COMSOL Multiphysics 5.0. This review's goal is to give a broad overview of the latest advancements in the main areas of microfluidic computations and the application of various COMSOL simulations, with a focus on biomedical engineering. Adam and Hashim [20] examined the latest developments in the application of several COMSOL simulations and significant types of microfluidic calculations, particularly in the biomedical engineering domain. In order to simulate a computational approach using the least squares method for finite elements across a rectangular channel enclosed within a semicircular cylinder with a Reynolds number between 100 and 1500, Khan et al. [21] looked into COMSOL Multiphysics 5.4. The Reynolds number used to analyze the flow pattern will be between 100 and 1000. They advise measuring the velocity and pressure before and after the cylinder. The percentage change in pressure and velocity before and after the cylinder was found to change their behavior for Re = 700. The comparison of the obtained results with the experimental data and results of the wellknown SST turbulence model, which is part of the COMSOL Multiphysics tool, was examined by Memon et al. [22]. Using a two-fluid turbulence model in COMSOL Multiphysics, Malikov et al. [23] examined flow behavior around aerodynamic profiles, highlighting the model's validation for precisely capturing intricate flow patterns pertinent to engineering and biomedical applications. Salem and Tuchin [24] looked into how blood flow patterns are important for diagnosing and treating cardiovascular diseases. In recent years, blood flow modeling has been widely used to better understand the variety of symptoms linked to different disorders. Wijayanti et al. [25] investigated how the chemical composition of wood parts greatly affected their physical properties. Among the biomass feedstocks used in the experiment, bamboo had the widest temperature distribution due to its unique properties. Hussain and et al. [26] looked at the temperature peaks at the edges, but it increases steadily as one crosses the top to the bottom border. A progressive decrease in the drag coefficient is observed near the walls, where maximum isothermal contour shapes are observed. In order to assess different fluidic and thermal properties, Ganie et al. [27] looked at five horizontal lines. They found that when the fluid collides with the screen, its velocity magnitude decreases at the bottom wall and increases at the higher wall. As a result, the highest walls show the biggest drop in pressure. This study presents the pressure distribution over the contracting portion and the range of velocity in the upstream and downstream sections of the pipe for Reynolds values of 372 and 968, respectively, as reported by Tarafder and Mia [28]. The results of experiments conducted with OpenFOAM and COMSOL Multiphysics are compared in this report. Malikov et al. [29] examined the use of Comsol Multiphysics applications and proved the superior accuracy, stability, and convergence of the two-fluid turbulence algorithm. Examining variables that impact fluid-particle interactions is the aim of this study. In their investigation of how altering the variables affects velocity, Marín et al. [30] present two distinct kinds of velocity profile plots: one orthogonal to the plates and one parallel to them.

Chapter 1 highlights about the basic concepts and definition used in this thesis.

Chapter 2 goes over the passage of a blood-based nanofluid through a stenotic artery containing gold and silver nanoparticles. The author addresses the impact of stenosis in an artery in this chapter, outlining how the stenotic region of the artery affects blood flow and how adding nanoparticles like gold and silver enhances fluid flow. It also talks about the changes in artery pressure and heat convection.

In Chapter 3 a CFD-based analysis of Newtonian nanofluid flow through a twodimensional channel with one and two solid circular cylinders is presented. The impact of thermal boundary conditions and the addition of nanoparticles on the flow characteristics is examined in this chapter. The evolution of convective patterns is examined in relation to temperature, pressure, velocity, and vortex dynamics, emphasizing the impact of obstruction geometry and heat conduction.

Chapter 1

Definitions

The fundamental definitions of key terms and concepts are covered in this chapter. This chapter piques the reader's interest and prepares them for a deeper exploration of the topic that follows.

1.1 Fluid

Substances with the ability to flow and change shape are called fluids. These consist of gases and liquids. No matter how much stress is applied, fluids can deform when sheared. When placed in a container, fluid molecules can replicate the shape of the container because they are not tightly held together, allowing them to move freely. Fluids include things like blood, water, and air.

1.2 Fluid Mechanics

1.2.1 The properties of fluids (liquids, gases, and plasmas) and the forces acting on them are the main topics of the physics discipline of fluid mechanics.

1.2.2 Types of Fluid Mechanics

Fluid Statics: Liquids at rest are the subject of fluid statics. It involves comprehending the forces that a static fluid applies to objects immersed in it as well as the variations in pressure in a resting fluid.

Fluid Dynamics: Fluid dynamics is the study of fluids in motion. It involves examining the forces causing the flow, its characteristics, and the consequences that follow. Three essential fluid dynamics equations are the Navier-Stokes equation, Bernoulli's equation, and the continuity equation.

1.2.3 Properties of Fluids

Some of the properties of fluids are given below

Density: Mass per unit volume is the definition of density. It is a measurement of the quantity of a matter's molecules in a specific area. A fluid's density is shown by

$$\rho = m/V \ . \tag{1.1}$$

Where ρ represent density of the fluid m is mass of fluid and V is volume of the fluid. It is usually expressed in kg/m^3 .

Viscosity: Viscosity is a fluid's resistance to flow or deformation. It calculates the fluid's internal friction as layers shift in relation to one another. The symbol for it is μ . Below is a discussion of viscosity types.

Dynamic Viscosity: The internal resistance of a fluid to flow when a force is applied is determined by its dynamic viscosity, also referred to as its absolute viscosity. It is defined as the ratio of the rate of shear strain to the shear stress. In terms of mathematics,

$$\mu = \frac{\tau}{\frac{du}{dy}} \ . \tag{1.2}$$

Kinematic Viscosity: Kinematic viscosity is defined as the fluid's dynamic (absolute) viscosity divided by its density. A fluid's resistance to flow and deformation under gravity is determined by its kinematic viscosity, a fundamental quantity in fluid dynamics. In terms of mathematics, it is represented as

$$v = \frac{\mu}{\rho} \,. \tag{1.3}$$

Pressure: The force applied to an object's surface per unit area is known as pressure. Having a magnitude but no direction, it is a scaler quantity. It can be expressed in a variety of units, including atmosphere (atm) and Pascal (pa). Its representation in mathematics is

$$P = \frac{F}{4} \,. \tag{1.4}$$

Where the pressure is denoted by P. A is the area over which the force was applied, and F is the applied force. When determining the behavior of fluids in fluid machines, including flow, buoyancy, and interaction with solid boundaries, pressure is a crucial factor.

Temperature: One essential physical parameter that shows the thermal state of a material or system is temperature. It calculates the average kinetic energy of a substance's constituent particles. The average kinetic energy of particles increases with temperature. Numerous scientific and technical domains, including fluid mechanics, thermodynamics, and materials science, depend on temperature.

1.2.4 Fluid Flow

The constant movement and deformation of fluid particles is known as fluid flow. It is the movement of energy, mass, and momentum within a fluid. The following is a list of the different types of flow.

Turbulent Flow: When a fluid moves erratically and chaotically, changing pressure and velocity, this is known as turbulent flow. It happens when there is an irregular object in the flow path or when the flow rate is higher.

Steady Flow: This kind of flow occurs when the fluid's characteristics, such as pressure and velocity, remain constant over time. At no point did the flow parameters alter over time.

Unsteady Flow: The flow in which the characteristics of the fluid change over time. Because the pressure and velocity vary over time, it is also referred to as time-dependent flow.

Compressible Flow: Compressible flow occurs when a fluid's density varies in response to temperature and pressure changes.

Incompressible Flow: An incompressible flow is one in which the fluid's density is unaffected by changes in pressure. Under all pressure conditions, the fluid's density stays constant.

Laminar Flow: When fluid particles travel at low velocity in a straight line parallel to pipe walls without layer disturbance, this is known as laminar flow or streamline flow. The type of flow in a tube is indicated by the Reynolds number. A Reynolds number of less than 2300 indicates laminar flow in a pipe. Laminar flow keeps the fluid's pressure, velocity, and other flow characteristics constant.

This type of flow is unusual in water systems.

1.2.5 Types of Fluids

Different types of fluids are mentioned below,

- Ideal fluids
- Inviscid fluids
- Real fluids
- Newtonian fluids
- Non-Newtonian fluids

Newtonian Fluids: Newton's law of viscosity, which states that the shear stress within a fluid is directly proportional to the shear rate, is followed by certain fluid types. Put simply, a Newtonian fluid's viscosity remains constant irrespective of the force applied. **Non-Newtonian Fluids:** Non-Newtonian fluids are those that do not adhere to Newton's law of viscosity. The viscosity of a non-Newtonian fluid varies as forces are applied. Dough, paint, and blood are a few non-Newtonian fluids.

Boundary Layer: A tiny area of fluid flow close to a solid surface that is greatly impacted by viscosity is known as the boundary layer. The fluid velocity in this layer shifts from zero (due to the solid boundary's no-slip condition) to freely flowing (fluid velocity above the surface).

Stagnation Point: A point in fluid flow where the fluid's velocity is zero is called a stagnation point. The fluid stops at this point, converting its kinetic energy to pressure energy.

Separation Point: The point in a fluid flow where the boundary layer separates from the surface of an object is called a separation point. The boundary layer thickens and eventually separates from the surface as a result of fluid particles close to the surface slowing down significantly due to an unfavorable pressure gradient.

1.3 Nanofluids

Synthetic fluids with nanoparticles dispersed throughout the base fluid are called nanofluids. These nanoparticles can be made of metals, oxides, carbides, or carbon nanotubes and range in size from 1 to 100 nanometers. Base fluids can include water, blood, oils, and other common heat transfer fluids. Compared to their base fluids, nanofluids have substantially higher thermal conductivities. The strong thermal conductivity of nanoparticles and their potential to increase heat transfer efficiency could be the cause of this increase. Convective heat transfer coefficients can be raised by adding nanoparticles, increasing the effectiveness of nanofluid in heating and cooling applications. Making sure the nanoparticles are uniformly distributed throughout the base fluid is crucial. Stability and agglomeration prevention are achieved through the use of surfactants, surface modification, and ultra-sonication. Depending on the kind and concentration of nanoparticles, a nanofluid may have a higher viscosity than base fluids. For certain applications, this necessitates careful

adjustment as it may affect flow characteristics. When compared to the base fluid, a nanofluid may exhibit unique thermophysical characteristics, such as differences in density, specific heat capacity, and thermal expansion coefficient. To sum up, nanofluids represent a major advancement in fluid technology, offering improved thermal properties and heat transfer capabilities for a variety of uses. However, challenges like stability, cost, and safety must be addressed if their potential is to be fully realized.

1.4 Equation of Continuity

The foundation of this equation is the principle of conservation of mass, which stipulates that the rate at which fluid mass increases within a volume must match the rate at which fluid mass enters or exits the surface area. In other words, a fluid's mass is only increased by flow through its surface area; no fluid is created or destroyed within a volume. The continuity equation that COMSOL Multiphysics uses is

$$\rho \nabla \cdot \mathbf{V} = 0 \ . \tag{1.5}$$

1.5 Navier-Stokes Equation

A group of nonlinear partial differential equations known as the Navier-Stokes equations are used to explain how viscous fluids move. Predicting fluid flow behavior requires the use of these equations, which account for density, viscosity, pressure, and velocity. Mathematically

$$\nabla \left(\frac{\partial \mathbf{V}}{\partial t} + \mathbf{V} \cdot \nabla \mathbf{V} \right) = -\nabla p + \mu \nabla^2 \mathbf{V} + f . \tag{1.6}$$

1.6 Bernoulli's Equation

Energy conservation in a fluid during its flow is addressed by Bernoulli's equation, a fluid dynamics principle. Its foundation is the conservation of energy, momentum, and mass. It implies that when a fluid's pressure or potential energy drops, the fluid's speed rises.

$$\mathbf{p} + \frac{1}{2}\rho \mathbf{v}^2 + \rho g h = constant \ . \tag{1.7}$$

1.7 Flow Measurement

The measurement of fluid velocity through channels is known as flow measurement. A venturimeter, which tracks variations in pressure, can identify it. Data is also gathered using mechanical flow meters, such as piston and turbine flow meters.

Volumetric Flow Rate

It is the volume of fluid that flows through a specific cross-sectional area in a second. m/s is the SI unit. Because mass and volume are related by density, volumetric flow rate is a subset of mass flow rate. To calculate, multiply the flow's cross-sectional area (A) by its average velocity (\dot{U})

$$\dot{U} = U_{avg} * A . \tag{1.8}$$

Mass Flow Rate

The amount of fluid that flows through a given area is referred to as the mass flow rate. kg/s is the unit. The volumetric flow rate and the mass flow rate are equivalent. It is calculated by multiplying volumetric flow by density.

$$\dot{M} = \rho * \dot{U}$$
, or
$$\dot{M} = \rho * U_{avg} * \mathbf{A} . \tag{1.9}$$

Fluid Velocity

The average speed of a pipe's cross-section is known as its average velocity. The average velocity is half of the maximum velocity for fully developed laminar pipe flow. When there is no slippage, the fluid velocity in the middle of a pipe increases from zero to its maximum. Because temperature affects density, heating and cooling fluids can alter their average velocity. In actuality, fluid characteristics are computed at a mean temperature and are regarded as constant.

$$U_{avg} = \frac{\dot{u}}{A} \,. \tag{1.10}$$

Heat Transfer

Temperature and heat flow are related to the phenomenon of heat transfer, where temperature denotes thermal energy and heat flow denotes the movement of thermal energy from a hotter to a colder body. Heat transmission is primarily caused by temperature differences.

• Conduction

Heat is transferred by conduction, which involves the movement of molecules and the kinetic energy exchange that goes along with it. Electricity is primarily carried by solids and static fluids. The concept of heat conduction, or Fourier's law, was first put forth by Joseph Fourier in 1822. It states that the heat flux resulting from thermal conduction has the opposite sign and is proportional to the size of the temperature gradient. has the opposite sign and is proportional to the temperature gradient's magnitude.

$$q = -k\frac{dT}{dx}. ag{1.11}$$

Where k represents thermal conductivity and the unit is W/m * k.

Convection

Heat flows as a result of convection, which happens when matter moves from a hot to a cool location. The idea of thermal convection, sometimes referred to as Newton's law of cooling, was created by Sir Isaac Newton in 1701. Newton's Law of Cooling states that the difference between an object's internal temperature and its ambient temperature determines how quickly its temperature changes.

$$q = C(T_{hody} - T_{fluid}). (1.12)$$

Where T_{body} is the temperature of the body.

 T_{fluid} is the temperature of the incoming fluid at constant body temperature.

C is heat transfer coefficient and the unit is $\frac{W}{m^2*k}$.

• Radiation

Emitting, transmitting, and absorbing energy from matter in the form of electromagnetic waves or particles is known as radiation. The radiation that a body emits is

$$Q = \epsilon \alpha A T^4 . \tag{1.13}$$

Here ϵ is emissivity of the body, α represent Stefan-Boltzmann constant, A is its total area and T is absolute temperature.

1.8 COMSOL Multiphysics

A comprehensive simulation software platform called COMSOL Multiphysics is used to model and resolve a variety of scientific and engineering issues. It is a vital tool for researchers and engineers in many fields, including fluid mechanics, because it uses finite element analysis (FEA) to solve complex physical phenomena. Fluid behavior is modeled and analyzed in fluid mechanics research using COMSOL Multiphysics. It can use finite element analysis to simulate heat transfer, fluid flow, and other related physical phenomena. Because it can handle complex geometries, boundary conditions,

and multiphysics interactions, this program is widely used in scientific and engineering research. The following lists some of COMSOL Multiphysics' key features and capabilities.

Multiphysics Simulation

Dealing with coupled and multi physics phenomena is the area of expertise for COMSOL Multiphysics. This makes it possible to use a single model to simulate multiple interacting physical processes. For instance, it is possible to simultaneously model structural mechanics, fluid flow, and heat transport.

Geometry and Meshing

Comprehensive tools for creating and importing complex geometries are available in COMSOL. Users can import geometries from other computer-aided design programs or use the integrated computer-aided design tools to create models from scratch. For precise simulation results, high-quality meshes are provided by the meshing tool.

Solver Technology

Numerous sophisticated solvers for both linear and nonlinear problems are included in COMSOL. Large-scale models with numerous degrees of freedom can be simulated thanks to these solvers' accuracy and efficiency.

Results and Visualization

The software offers robust postprocessing capabilities for viewing the outcomes of simulations. The creation of plots, animations, and data exports makes it simple for users to evaluate or communicate their findings. In fluid mechanics studies, surface plots, contour plots, and streamline plots are especially helpful.

Modules

Numerous specially designed modules aimed at specific applications are offered by COMSOL. COMSOL Multiphysics can be used to discuss fluid mechanics modules such as heat transfer, microfluids, and computational fluid dynamics (CFD).

1.8.1 Application of COMSOL Multiphysics in Fluid Mechanics:

Flow Analysis

Laminar and turbulent flows, single and multiphase flows, and compressible and incompressible flows are all frequently simulated using COMSOL Multiphysics. Numerous boundary conditions are supported by the software, such as periodic boundaries, no-slip and slip conditions, and inlet and outlet conditions.

Multiphase Flow

Liquid-liquid, gas-liquid, and gas-solid interactions are among the fluid phase interactions that the software can model. This is essential to comprehending processes like droplet formation, boiling, and cavitation.

Microfluids

The Microfluidics Module makes it possible to simulate fluid behavior at the microscale. This is particularly crucial for micro-scale heat exchangers, biomedical applications, and lab-on-a-chip systems.

Chapter 2

Numerical Investigation of Blood Flow on Hybrid Nanofluid with Heat Transfer through a Curvy Stenotic Artery: Silver and Gold

2.1 Introduction

The proposed study examines the numerical modeling of a hybrid nanofluid containing gold and silver nanoparticles across a stenotic artery using COMSOL Multiphysics, a CFD tool. In this study, blood is used as the base fluid. The flow is depicted as suitable at high shear rates due to the Newtonian nature of the blood and its incompressible, laminar flow. The performance of blood flow in response to changes in heat, pressure, and velocity caused by stenotic arteries was examined. Gold and silver nanoparticles were used in this work. A mass, velocity, and energy algorithm was developed using the computational fluid dynamics (CFD) approach. COMSOL Multiphysics was used to create a fine element size mesh.

2.2 Mathematical Modeling

An incompressible Newtonian fluid passing through a stenosed artery is the fluid used in this investigation. Ag and Au nanoparticles are added to blood, which serves as the base fluid. Blood flow through a stenotic artery is depicted in Fig. (2.1.) The coordinates were chosen so that the blood flow perpendicular to the flow was taken into consideration in the direction of the r and z-axis. The stenosed area has a radius of 0.4 meters and a height of one, giving it a cosine shape. With coordinates r = -1.2 and z = -0.35, the 2D artery is 2.5 m long and 0.8 m high. The add physics tool is used to incorporate heat transfer and laminar flow into COMSOL Multiphysics 6.1. The velocity at the boundary was zero, and the inlet and outlet were identified. 310K is the

typical temperature for heat transfer and laminar flow. With temperature 1 at the upper boundary of 298K and temperature 2 at the lower boundary of 300.5K, the initial heat transfer temperature was 273K. Properties of blood material were discussed. Mass, velocity, and the thermal expansion equation are among the time-dependent equations that are employed.

Continuity Equation

$$\frac{1}{r}(ru)_r + w_z = 0, (2.1)$$

The continuity is written in COMSOL Multiphysics as

$$\nabla . V = 0, \tag{2.2}$$

The velocities u and v are in the x and y-axis respectively

Equation of Momentum:

$$\rho_{hnf}(u_t + uu_r + wu_z) = -p_r + \partial_z(w_r - u_z)\mu_{hnf}, \tag{2.3}$$

$$\rho_{hnf}(w_t + uw_r + ww_z) = -p_z - \left(\partial_r + \frac{1}{r}\right)(w_r - u_z)\mu_{hnf}.$$
 (2.4)

The momentum equation's governing model

$$\rho \frac{\partial \mathbf{V}}{\partial t} + \rho(\mathbf{V}.\nabla)\mathbf{V} = \nabla \cdot [-PI + \mathbf{K}] + F, \tag{2.5}$$

$$K = \mu(\nabla V + (\nabla V)^T). \tag{2.6}$$

In this equation, ρ_{hnf} represents the density of the nanofluid, μ_{hnf} represents its viscosity and P represents the fluid's pressure.

Equation of Energy

$$(\rho C_P)_{hnf}(\partial_t + w\partial_z + u\partial_r)T = k_{hnf}(\partial_{rr} + r\partial_r + \partial_{zz})T. \tag{2.7}$$

The controlling heat transfer equation is:

$$d_z(\rho C_p) \left(\frac{\partial T}{\partial t}\right) + d_z \rho C_P V \cdot \nabla T + \nabla \cdot q = d_z Q + q_0 + d_z Q_p + d_z Q_{vd}, \tag{2.8}$$

where $Q_{vd} = \tau \nabla V$ denotes the viscous dissipation heat source $\tau = -PI + K$,

 $q=-d_z k \nabla T$. Here Q denotes heat source ∇T denotes Temperature differential and d_z is thickness of fluid.

Initial Values

$$u = 0$$
, $w = 0$, $T = T_0$, and $P = 0$. (2.9)

The thermophysical features of nanofluid with nanoparticles in it are defined:

$$\rho_{hnf} = (1 - \phi_2) [(1 - \phi_1)\rho_f + \phi_1\rho_{s1}] + \phi_2\rho_{s2} ,$$

$$\mu_{hnf} = \frac{\mu_f}{(1 - \phi_1)^{2.5}(1 - \phi_2)^{2.5}} ,$$

$$(\rho C_P)_{hnf} = (1 - \phi_2) [(1 - \phi_1(\rho C_P)_f + \phi_1(\rho C_P)_{s1}] + (\rho C_P)_{s2}\phi_2,$$

$$\frac{k_{hnf}}{k_f} = \frac{k_{s1} + 2k_f - 2\phi_1(k_f - k_{s1})}{k_{s1} + 2k_f + \phi_1(k_f - k_{s1})} * \frac{k_{s2} + 2k_f - 2\phi_2(k_f - k_{s2})}{k_{s2} + 2k_f + \phi_2(k_f - k_{s2})}.$$
(2.10)

Geometry of the Stenotic Artery: the geometry of 2D stenotic artery in COMSOL Multiphysics.

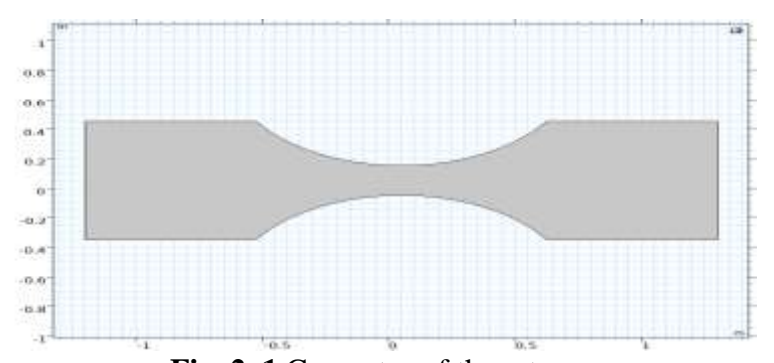


Fig. 2. 1 Geometry of the artery.

Boundary Conditions

The boundary condition was consisting of inlet, outlet, walls and thermal insulation.

The Inlet

The blood circulation rate was determined at the artery's entrance. The area of the inflow route and the intake velocity can be used to modify the blood volume. The selection of the system's intake is shown in Fig. (2. 2.). This is the boundary condition at an artery's inlet.

$$u(r,z,t) = -u_0 n. (2.11)$$

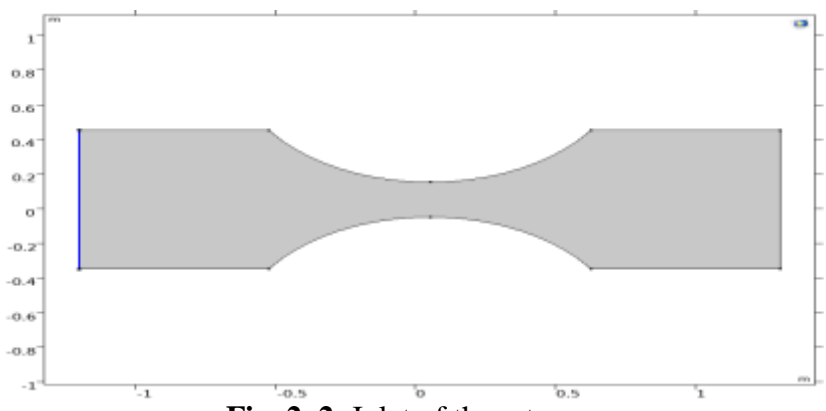
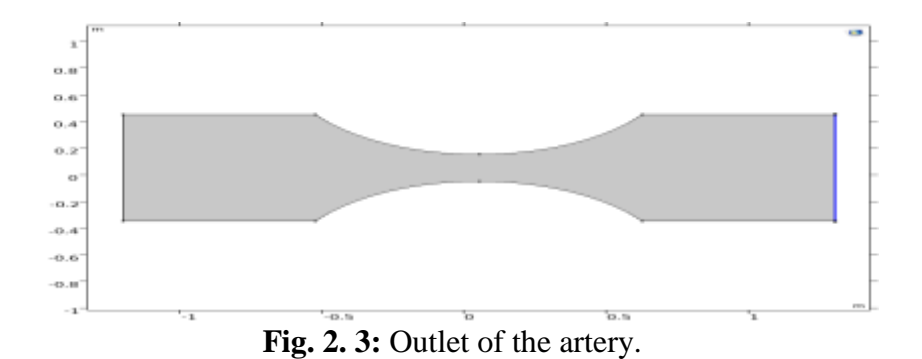


Fig. 2. 2: Inlet of the artery.

The Outlet

Pressure at the outflow is included in the model to guarantee realism. Fig. (2.3.) depicted the outlet, where the blood exited. It stood on the other side of the door.

$$[-PI+K]n = -P_0n, \quad where \quad P_0 \le P. \tag{2.12}$$



Walls of the Stenotic Artery

Because blood is so viscous, it cannot pass through the walls. At the wall, the boundary and no-slip conditions were then established. The arterial walls are shown in Fig. (2.4.)



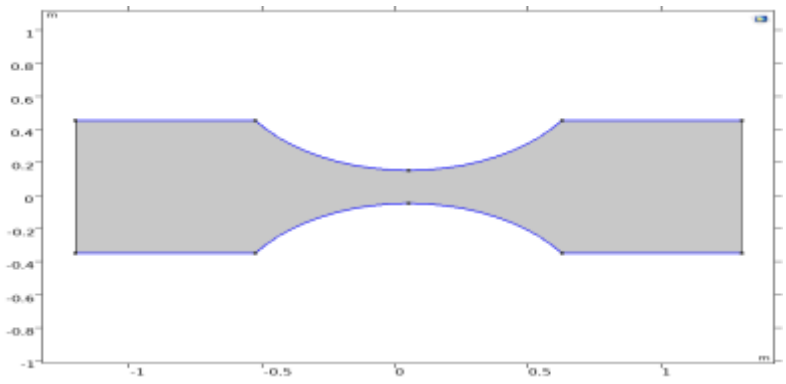


Fig. 2. 4: Walls of the stenotic artery.

Thermal Insulation

Fig. (2.5.) displays the insulating boundaries in the COMSOL heat transfer module.

Thermal insulation equation in COMSOL was:

$$-n. q = 0.$$
 (2.14)

Temperature: Temperatures of the stenotic artery walls are given below;

Temperature 1: Temperature at upper boundary of stenotic artery is shown in Fig. (2.6.)

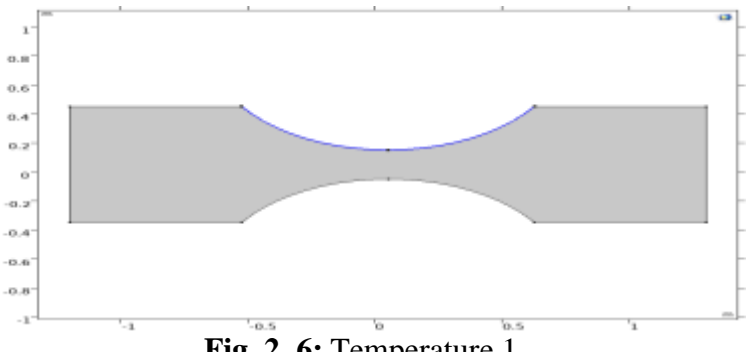


Fig. 2. 6: Temperature 1.

Temperature 2: Temperature at the lower boundary of the artery wall is shown in Fig. (2.7.)

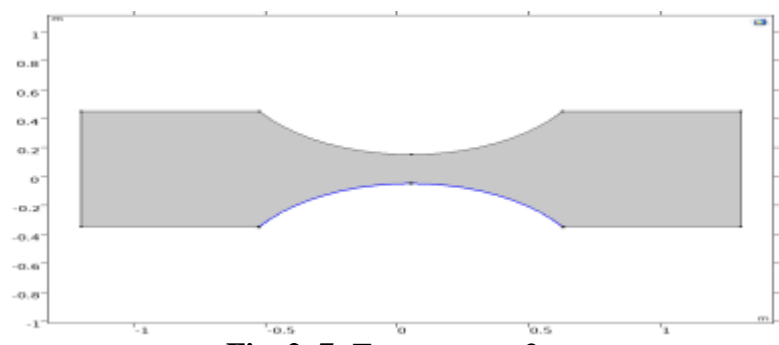


Fig. 2. 7: Temperature 2.

Computational Mesh

A mesh is an essential part of CFD. The mesh quality affects both the rate of convergence and the accuracy of the solution. COMSOL's "physics driven mesh" is used to create the mesh automatically. Fine element size mesh performs better and yields more accurate results than standard size mesh. A fine element size mesh is shown in Fig. (2.8).

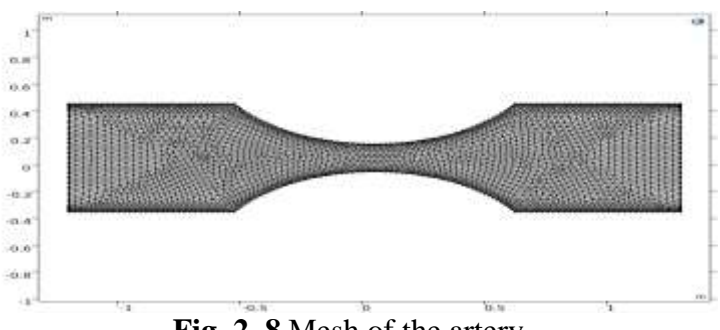


Fig. 2. 8 Mesh of the artery.

2.3 Results and Discussion

A mesh is an essential part of CFD. The mesh quality affects both the rate of convergence and the accuracy of the solution. COMSOL's "physics driven mesh" is used to create the mesh automatically. Fine element size mesh performs better and yields more accurate results than standard size mesh. A fine element size mesh is shown in Fig. (2.8).

Surface Velocity Magnitude

Fig. 2.9(a—d) displays magnitude of velocity at surface of artery for time intervals of 0.2, 0.8, 1.2, and 2 seconds.

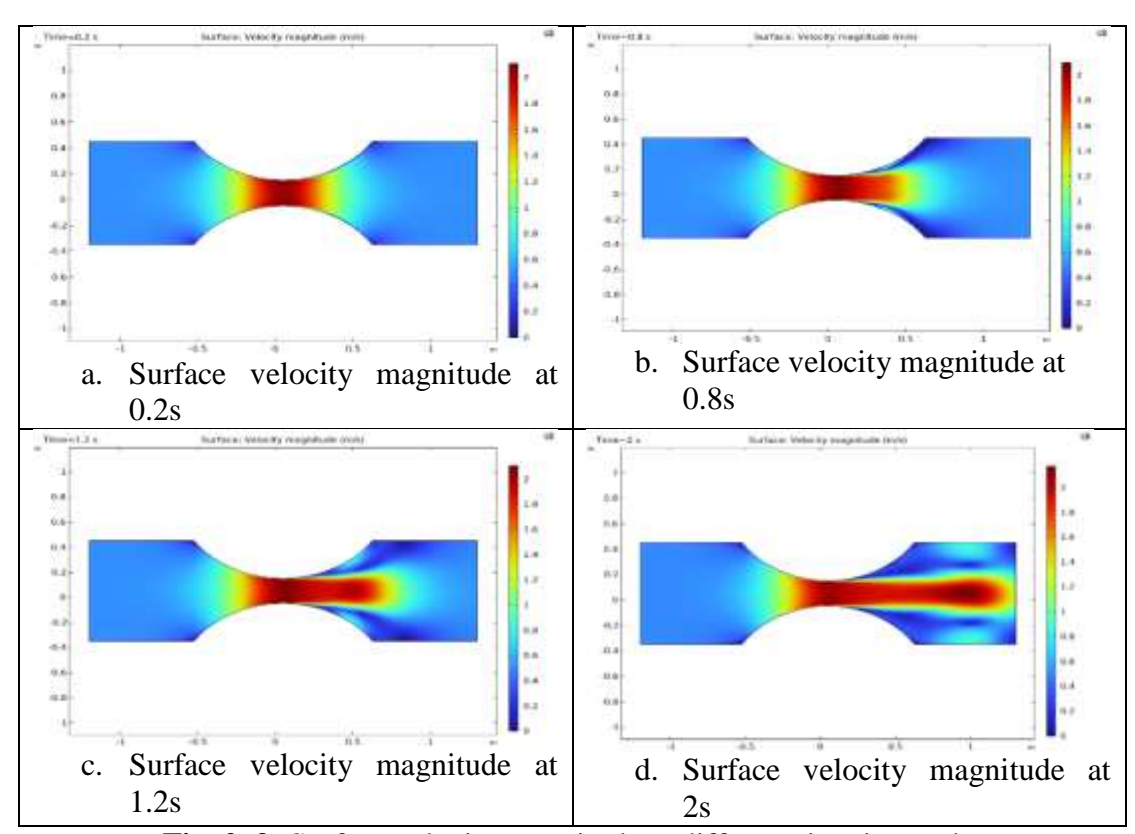


Fig. 2. 9: Surface velocity magnitude at different time intervals.

In the first stage, blood flow that is moving freely undergoes contraction at a specific point in the artery, resulting in an abrupt increase in velocity along a particular path, as seen in Fig. 2.9(a). where the stenotic artery's center has a peak velocity of about 2.1

m/s at 0.2 s. The velocity at 0.8 seconds is displayed in Fig. 2.9(b), which also notes that the flow begins to disperse as it leaves the stenosed area. The top and lower edges of the stenosed artery have the highest surface velocity, which is approximately 0.2 m/s. At 1.2 seconds, as shown in Fig. 2.9(c), the surface velocity increased by 0.01% over previous times, and swirling motions were seen when the nanofluid's motion was at its maximum. Lastly, Fig. 2.9(d) shows that blood circulation increases as nanofluids pass the stenosed area, putting more pressure on the arterial walls. While lower velocities of 0.7 m/s are seen just beneath and above the upper and lower artery walls, the center exhibits the highest surface velocity of 1.8 m/s.

Velocity Surface Plot in Vertical and Horizontal Directions

The velocity profile at times 0.2s, 0.8s, 1.2s and 2s is shown in Fig. 2.10(a-d) respectively.

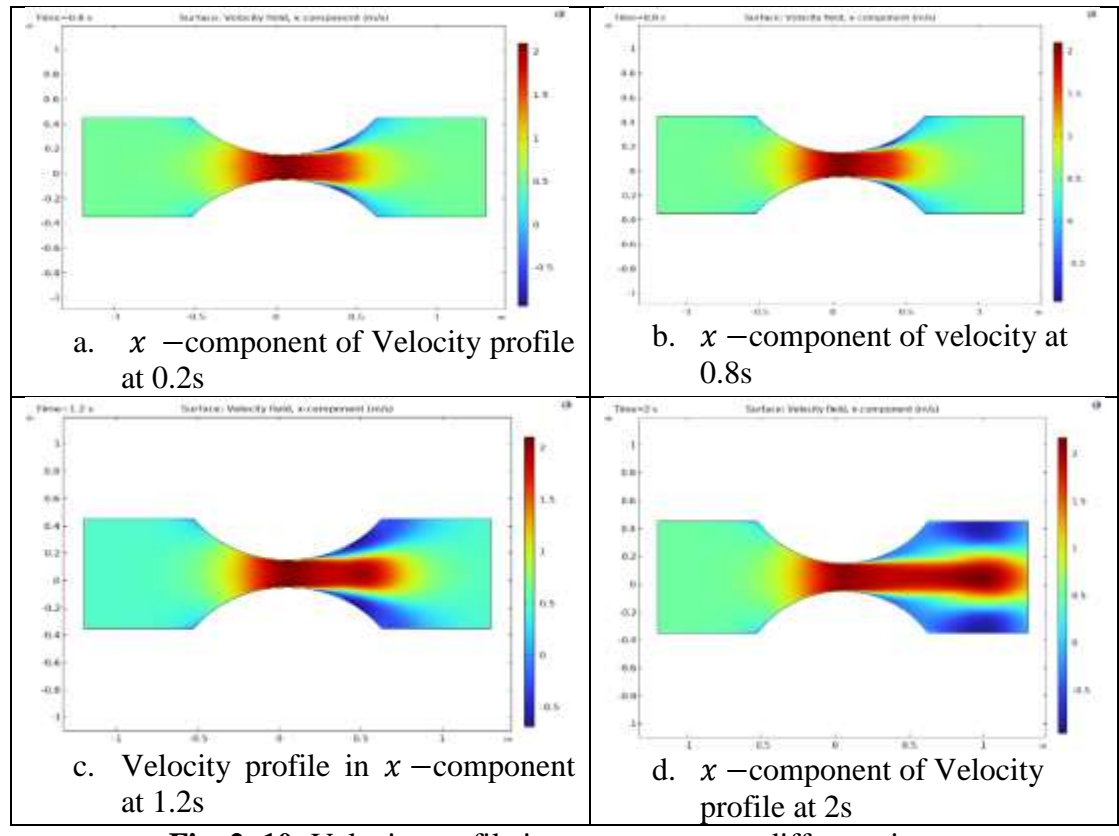


Fig. 2. 10: Velocity profile in x-component at different times.

Fig. 2.11 (a—d) depicts the vertical velocity profile (y-axis) at times 0.2s, 0.8s, 1.2s, and 2s.

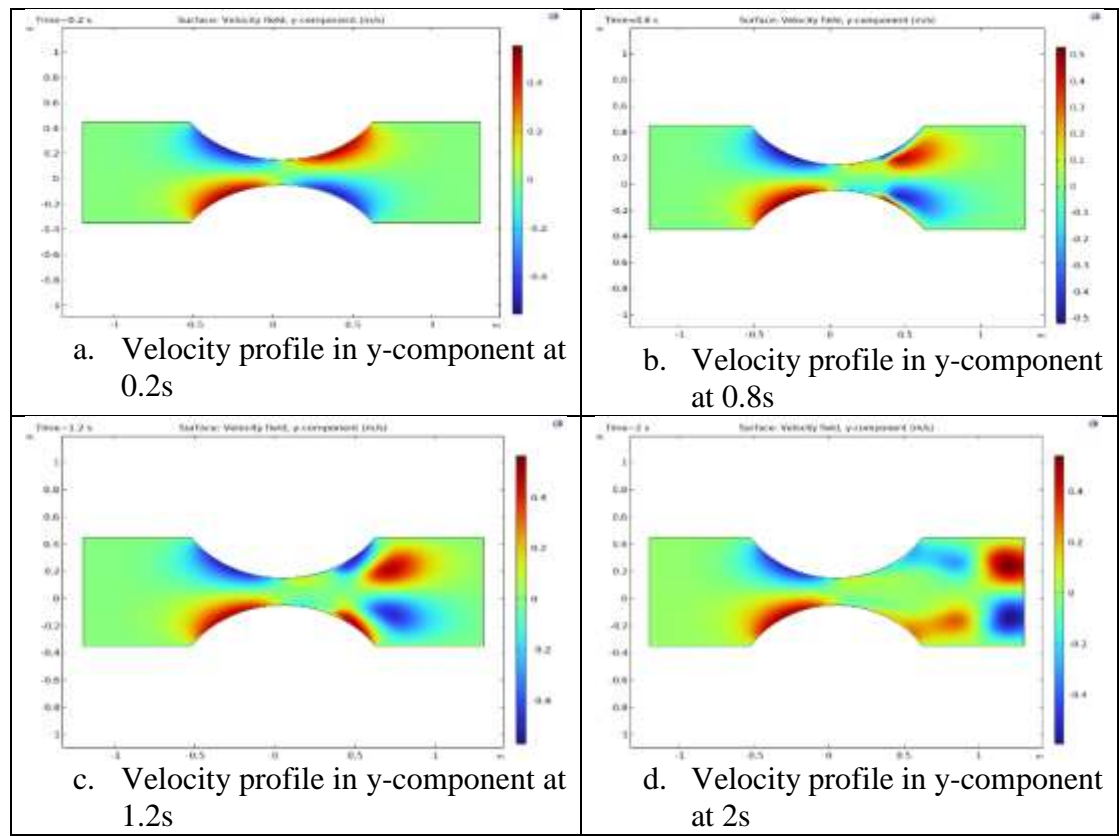


Fig. 2. 11: Velocity profile in y-component at different times.

The velocity profile reached its maximum velocity of 2.11 m/s along the x-axis at 2 s, and the minimal surface velocity of the stenosis is 2.11 m/s at 0.8 s. Fig. 2.11(a—d) illustrates how stenosis affects nanofluid movement along y-direction. It is crucial to note that the free-flowing blood-based nanofluid exhibits significant before and after stenosis artery motion. The velocity of the blood-based nanofluid abruptly increased after passing through the narrowed region of the artery. This indicates that the pressure applied to the artery walls has increased in the center of flow configuration due to the increased mobility of the nanofluid. The surface velocity curve in the y-direction at 0.2 s is displayed in Fig. 2.11(a). The surface velocity in the y-direction is 0.45 m/s for 0.2 s. Remarkably, the lower starting point of stenosis has the highest surface velocity,

while the upper curved surface has the lowest. The velocity profile along the y-axis at 0.8 s is shown in Fig. 2.11(b), where the magnitude of the surface velocity has decreased. The maximum surface magnitude was 0.42 m/s at 0.8 seconds. The magnitudes of the velocity profile at 1.2 and 2 seconds are shown simultaneously in Fig. 2.11(c,d). As seen in Fig. 2.11(c,d), the magnitude of the velocity profile has increased to 0.45 m/s at 1.2 s, and this increase is demonstrated to continue for the durations from 1.2 s to 2 s.

Pressure Profile

Pressure levels of nanofluid flow through the constricted artery is shown in Fig. 2.12(a—d) at various intervals: 0.2, 0.8, 1.2, and 2 seconds.

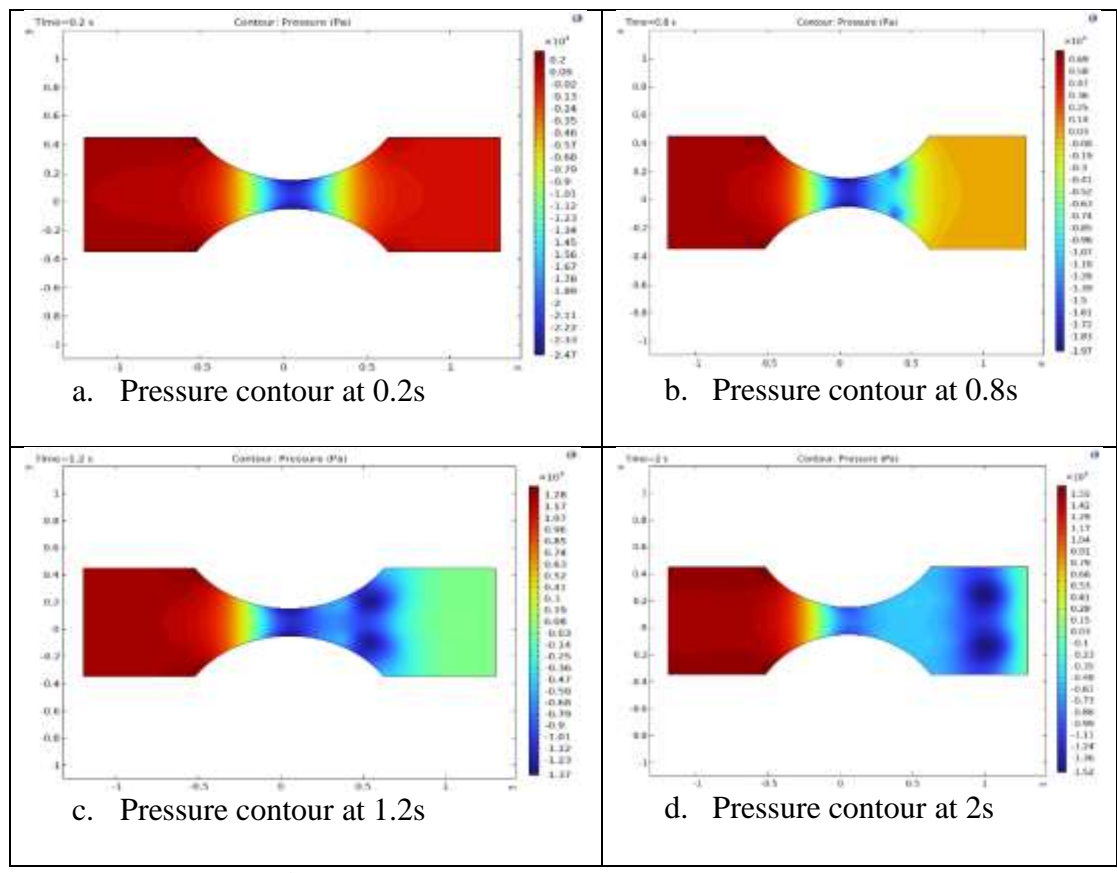


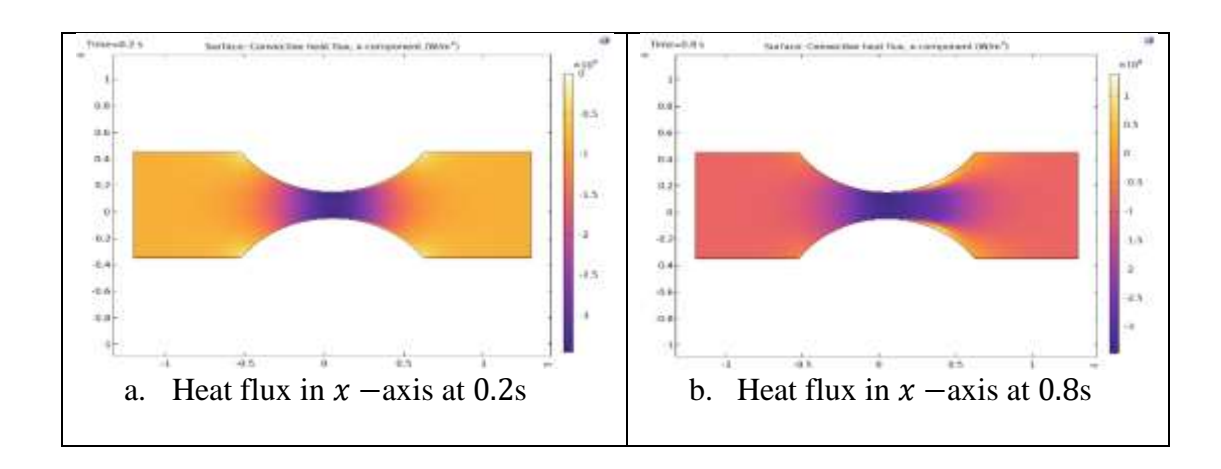
Fig. 2. 12: Pressure contour at different times.

Fig. 2.12(a) illustrates the pressure that a contracted artery experiences at its wall due to the motion of nanofluid. It is evident that at the start of the contraction, the pressure

profile peaked at 0.2 Pa. It should be noted that the free-flowing fluid reached the middle of the stenosis structure at which point the lowest pressure was measured. This implies that there is very little pressure above and below the walls because the fluid containing the nanoparticles is moving at its fastest speed in the center of the contraction. Fig. 2.12(b) displays the pressure profile at 0.8 s. The center of the stenosis exhibits a low-pressure profile, and the applied pressure has abruptly increased to 0.69 Pa. At time 1.2 s, the pressure profile rapidly increased, as seen in Fig. 2.12(c). More blood-based motion is the cause of this elevated pressure profile phenomenon. The pressure profile for the two-second time interval region is shown in Figure 2.12(d). Additionally, the lowest pressure drops to -0.42 Pa when 1.78 Pa more pressure is applied. Notably, the swirling motion of the nanofluid intensified in proximity to the outlet wall. Additionally, it has been found that the only factor contributing to the increase in pressure is the location of the restricted artery.

Convective Heat Flux

Fig. 2.13 (a—d) depicts convective heat flux at the x —coordinates within the stenotic area across time intervals of 0.2, 0.8, 1.2, and 2 seconds.



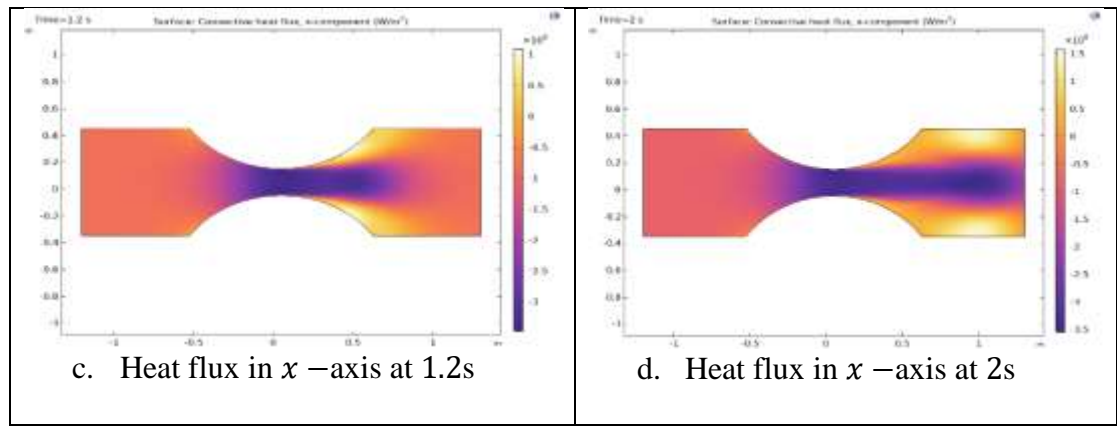


Fig. 2. 13: Convective heat flux at x axis for different times.

As seen in Fig. 2.13(a), the convective heat transfer during 0.2s shows that the artery's stenotic zone along the x-direction had the least amount of heat flux, while the boundary of the purported cavity had the highest heat flow due to convection. The convective heat flux at 0.8 s is displayed in Fig. 2.13(b). The area with the lowest heat flux along the x-direction has risen due to convection; the area with the lowest heat flux is now close to the artery wall. The convective heat flow for 0.8 seconds is shown in Fig. 2.13(b). Maximum heat flux is now visible at the cavity walls, as convection has expanded the area with the lowest heat flux along the x-direction (see Fig. 2.13(b)). The convective heat flux for time 1.2 seconds is shown in Fig. 2.13(c). Using blood as the base fluid, the profile shows that increased nanofluid mobility has caused the smallest region of the convective heat flow pattern within the x-axis to grow. Additionally, the top and bottom walls of the configuration have the highest convection. Convective heat flux is shown for two seconds in Fig. 2.13(d). This illustrates how the velocity of the nanofluid increases in the center of the artery. As can be seen in the center of the configuration, this profile indicates that the nanofluid's velocity increased, and the maximum heat flux across the x-axis was recorded at 1.84E8. Additionally, it is observed that the convective heat flow is getting closer to both its minimum of -3.5E8 and its maximum of 1.85E8 at 2 seconds.

Fig. 2.14 (a—d) depicts convective heat flux across y —direction in intervals at 0.2, 0.8, 1.2, and 2 seconds.

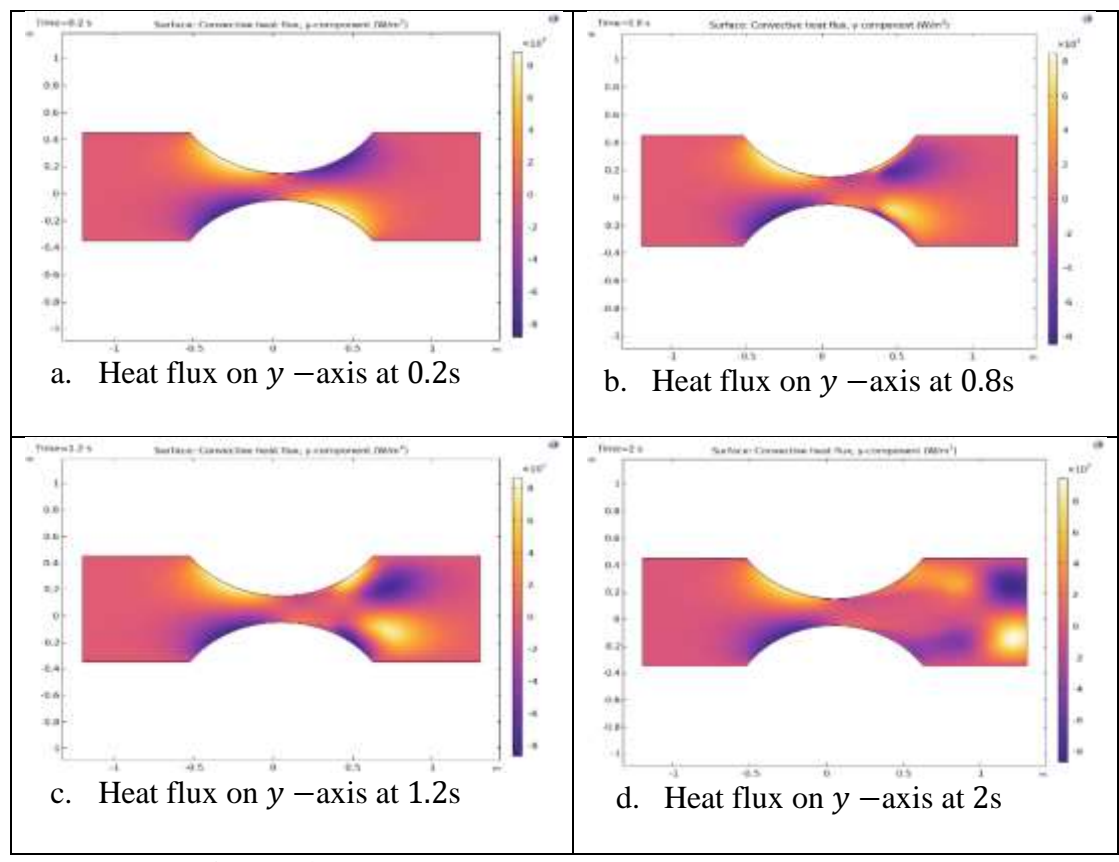


Fig. 2. 14: Heat flux at y –axis at different time intervals.

It is noteworthy that there are similarities between the surface magnitude profiles and convective heat flow patterns along the y-direction. The results demonstrate that convection requires blood-based fluid mobility in the y-direction. According to Fig. 2.14(a), the constricted artery's convective heat flux is highest at the higher beginning points and lowest at the lower end points. 1.25E8 was the highest convective heat flux recorded at 0.2 seconds. Convective heat flux along the y-direction at time 0.8 s is shown in Fig. 2.14(b). As the convective area of flow increases, the heat flux reaches 1.22E8, as seen in Fig. 2.14(b)). The convective flow of heat along the y-direction for 0.8 seconds is shown in Fig. 2.14(b). Heat flux produced by convection along the y-direction at 1.2 s is displayed in Fig. 2.14(c). At 1.2 s, the addition of nanofluid decreased heat flux along the y-direction. Additionally, a diffused convective heat flux

was observed along the y-axis at 2 seconds. 1.16E8 was the maximum heat flow measured. The slow velocity of the blood-based nanofluid caused a decrease in the y-direction heat flow profile. The limited area has the lowest heat flux, according to the convective heat flow patterns for the x and y directions; however, smoother motion results in higher heat flux profiles for nanofluids. Figure 2.14(b).

Surface Temperature

The surface temperature of the flow is shown in fig. 2.15(a—d) at 0.2s, 0.8s, 1.2s and 2s respectively.

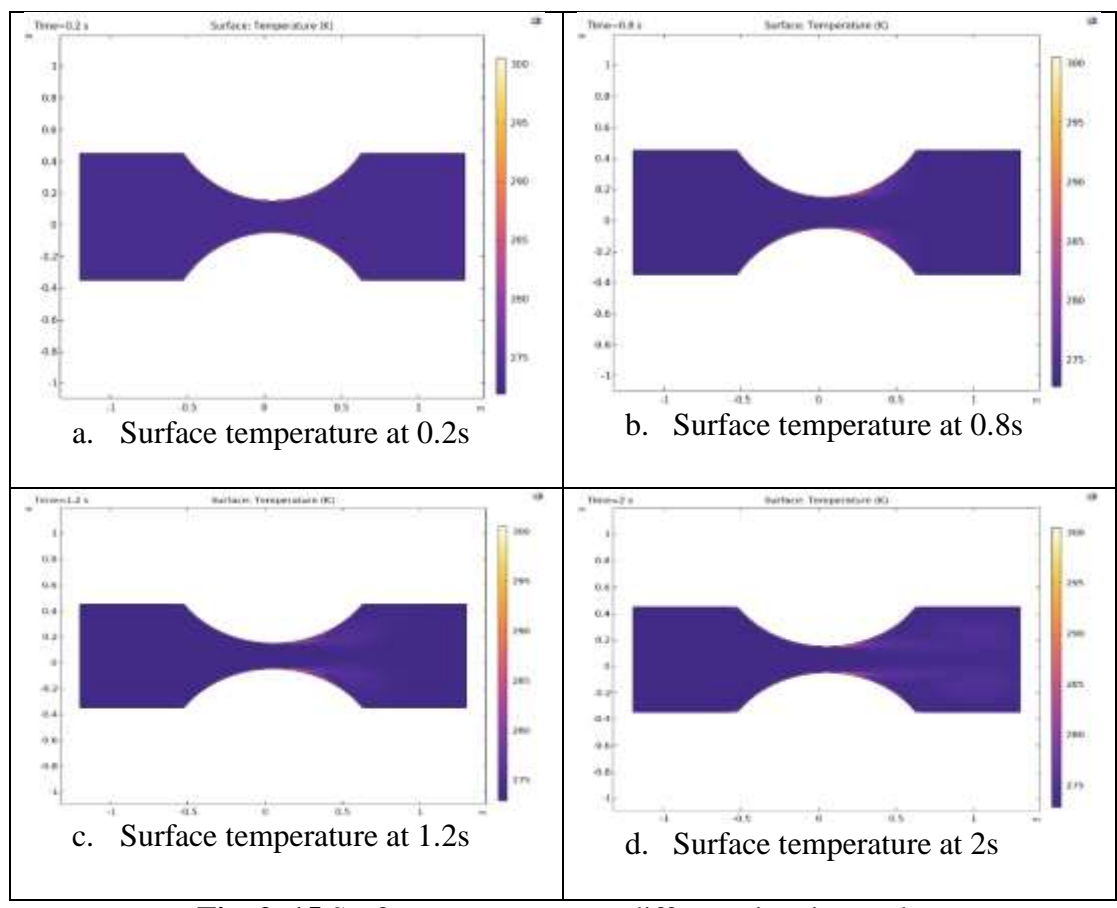


Fig. 2. 15 Surface temperature at different time intervals.

The highest surface temperatures were found at the stenotic artery's upper and lower borders. Between them, the temperature varies between 265K and 275K. The surface temperature of the artery's upper and lower boundaries rises with time, as seen in Fig.

2.15(a—d). The upper and lower boundaries each had a maximum surface temperature of 295 K prior to contraction.

Temperature Contour

Fig. 2.16(a—d) shows temperature contours at 0.2, 0.8, 1.2 and 2 seconds respectively.

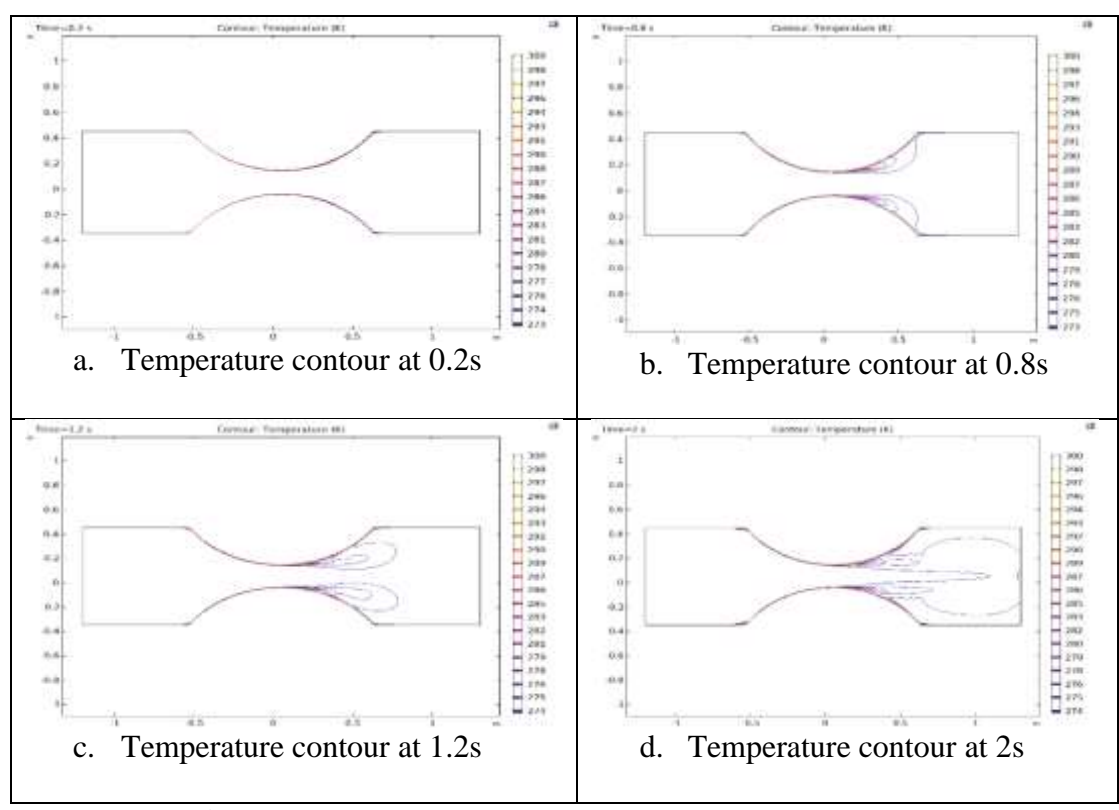


Fig. 2. 16 Temperature contours at different time intervals.

The greatest number of isothermal contours occurs at 2s, whereas the fewest occurs at 0.2s. The nanofluid's velocity rises with time, creating a larger isothermal contour.

Streamline

Fig. 2.17(a—d) depicts the streamlines of current problem at various points in time.

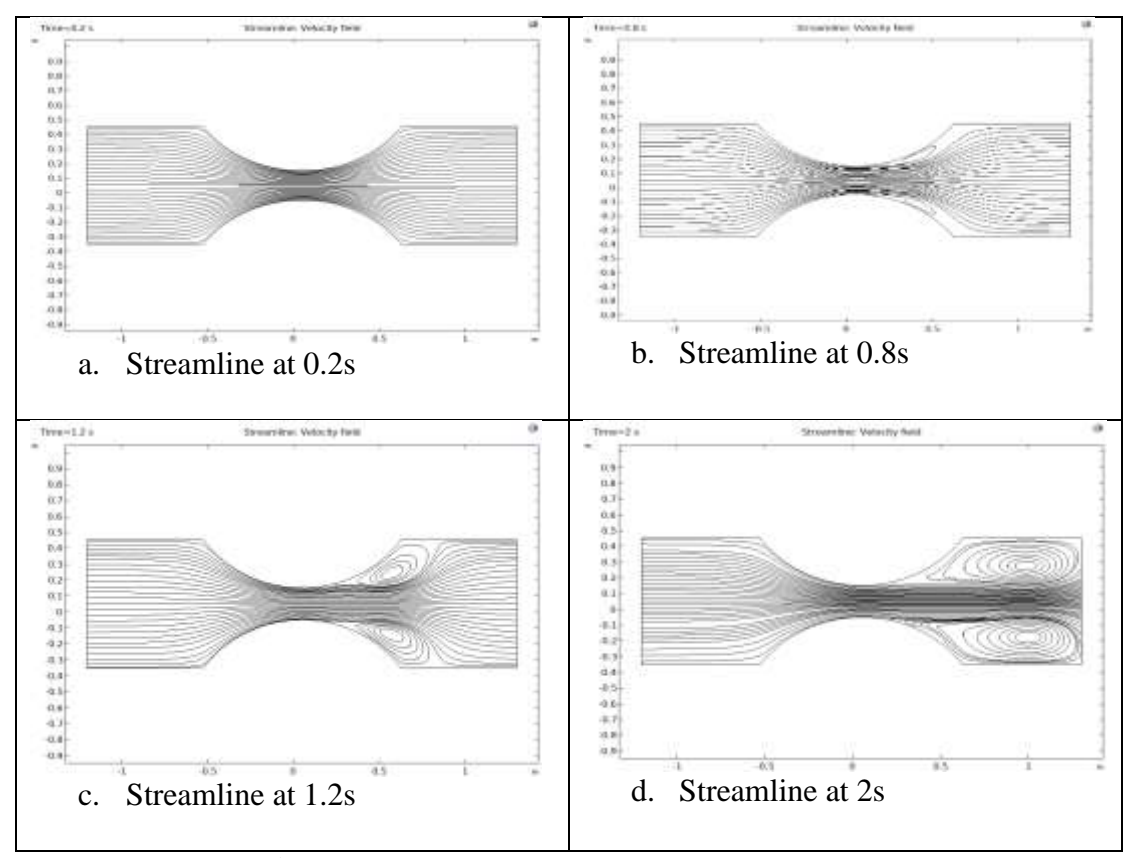


Fig. 2. 17 Streamlines at different time intervals.

The motion produced by a flowing fluid at any given time is represented by predefined lines in streamlines. The streamlines for time 0.2 s are shown in Fig. 2.17(a). In streamlines, smooth flow patterns had been discovered. As it passes through the stenosis, the blood-based nanofluid starts to spread out the streamline pattern at 0.8 seconds, as seen in Fig. 2.17(b). The streamlines shape for 1.2 seconds is shown in Fig. 2.17(c). After narrowing, the streamline profile shows the swirling motion of the surface velocity distribution. The streamlines at 2 s are shown in Fig. 2.17(d). When the stenosis bends, the whirling motion is more apparent. Additionally, the stenosis artery's streamline route is disrupted by the nanofluid's rapid movement.

Table. 2. 1 Display the thermophysical characters of the base fluid and nanoparticles.

Properties	Density	Heat capacity	Thermal conductivity	Dynamic Viscosity
Blood	1063	3746	0.52	0.003
silver	10500	235	429	0.005
gold	19300	129	310	0.00464

Table. 2. 2 Mesh size and mesh properties.

		Recent work
Elements	Mesh 1	Mesh 2
Element Size	Normal	Finer
Mesh Area	$0.5949 \ m^2$	$0.5948m^2$

2.4 Conclusion

The finite difference method (FDM) was used to derive the numerical solution for the study, which concentrated on the Newtonian properties of blood. Blood, gold, and silver make up mixed nanofluid. Numerical solutions and mathematical models are essential for predicting the causes of atherosclerosis, and the proposed study indicates that nanoparticle technology may offer a viable treatment option for arterial issues. Furthermore, the current study has the potential to reveal crucial elements that are significant for biological applications. The following are the main findings:

- Blood flow can be enhanced by adding nanoparticles to the circulation.
- The laminar flow study showed that variations in blood flow velocity throughout the model are caused by arterial plaque.

- As the severity of the stenosis increased, streamlines in the affected area showed unusual behavior and needed to be reevaluated. To restore regular flow, nanoparticles were added.
- As time goes on, the fluid's temperature and heat fluctuate.
- The pressure of the fluid is low at the stenosed region.
- To determine the causes of stenosis, the study looks at physical characteristics like the skin friction coefficient, MHD (Magnetohydrodynamics), and radiation effects. This may help treat vascular stenosis.
- Gold and silver nanoparticles improve stenosis hemodynamics.

Chapter 3

Effect of Thermal Boundary Condition on the Convective

Flow of Nano Fluid Through a Cylinder

3.1 Introduction

In this chapter, a Computational Fluid Dynamics (CFD) analysis using COMSOL Multiphysics is presented to investigate the impact of thermal boundary conditions on convective nanofluid flow through a two-dimensional circular cylinder arrangement. The flow past a circular cylinder is one of the most basic and extensively studied fluid mechanics problems; it serves as the foundation for knowledge of heat transfer behavior, wake formation, and vortex shedding. To validate the model and set a baseline for both hydrodynamic and thermal performance, the classical case of flow past a single solid obstacle is first simulated. The benchmark model found in the COMSOL Application Library [33] serves as the foundation for the configuration. In order to examine the effects of multiple obstacles on flow separation, recirculation zones, and convective heat transfer, the model is then expanded to incorporate a second solid obstacle inside the confined channel. To improve thermal conductivity, an incompressible, Newtonian nanofluid made of copper nanoparticles suspended in water is employed as the working fluid. Both cylinders are subjected to hot wall boundaries and a fixed inlet temperature in order to simulate realistic heat transfer conditions; the remaining walls are regarded as adiabatic. Time-dependent simulation is used to investigate the impact of these thermal gradients, capturing both the domain's heat propagation and transient flow behavior. Particle tracing is also used to visualize fluid motion and record the response of flow containing nanoparticles to thermal effects and solid boundaries. In line with earlier research involving sinusoidal ridges and magnetohydrodynamic effects, it is demonstrated that the presence of two obstacles causes a greater disruption of the streamlines, resulting in improved mixing and localized heat transfer. This numerical study offers a strong foundation for evaluating the joint effects of thermal boundary conditions, dual geometrical blockage, and nanofluid enhancement on confined laminar flow.

3.2 Mathematical Modelling

According to the study, a Newtonian incompressible nanofluid passes through a two-dimensional circular conduit that has one or two solid obstacles in it. In COMSOL Multiphysics, the geometry is created to study the behavior of heat transfer and flow. The channel's structure with one obstacle inserted inside is depicted in Figure (3.1.) It is believed that the nanofluid travels along the x and y axes. The domain is 0.2 meters high and 1 meter long. Each cylinder is positioned at a certain spot within the channel and has a radius of 0.05 m. The nanofluid is created by adding copper (Cu) nanoparticles to water, which serves as the base fluid. It is assumed that the flow is steady and laminar. The temperature at the inlet boundary is 300 K, and the surface boundary of both cylinders are set at 350 K. These are the thermal boundary conditions. The remaining barriers are regarded as adiabatic, meaning they do not transfer heat. All walls are subject to no-slip conditions, which means that the fluid's velocity at these limits is zero.

The incorporate Physics tool in COMSOL is used to incorporate the physics of heat transport and fluid flow. To track the temperature change and velocity variation over time, a time-dependent research is chosen. To observe how particles travel with the flow, particle tracing is also incorporated. The simulation demonstrates how the nanofluid responds to temperature changes and how the two obstacles' presence impacts

heat transfer and flow. This mathematical model is adapted and extended from the Flow past a cylinder application example provided in the COMSOL Multiphysics Application Library [33].

General Geometry of Flow

A two-dimensional image of the flow geometry with single solid obstacle introduced is displayed in Figure (3.1.) [33].

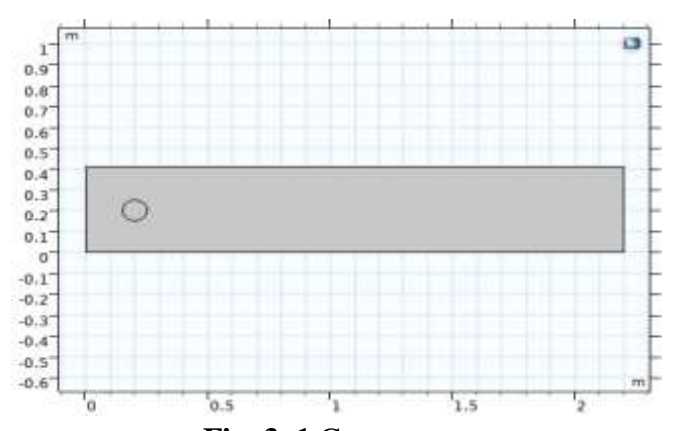


Fig. 3. 1 Geometry.

Similarly A two-dimensional image of the flow geometry with two solid obstacles introduced is displayed in Figure (3.2.)

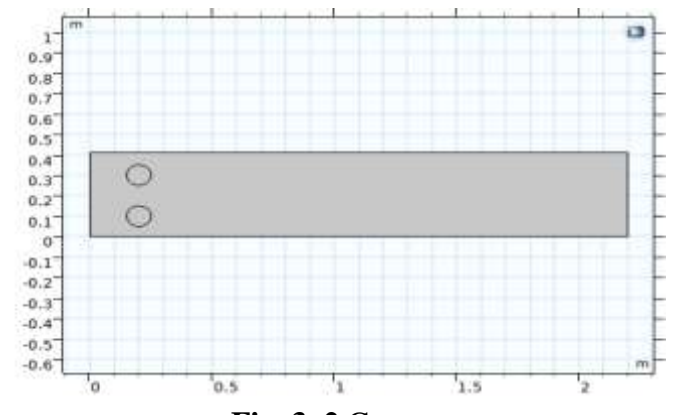


Fig. 3. 2 Geometry.

Equation of Continuity

$$\frac{1}{r}(ru)_r + w_z = 0. ag{3.1}$$

In COMSOL, the continuity equation is expressed as

$$\nabla \cdot \mathbf{V} = 0. \tag{3.2}$$

The velocities u and w are in the r and z —axis respectively.

Momentum equation

$$\rho_{nf}(u_t + uu_r + wu_z) = -p_r + \mu_{nf} \left(\nabla^2 u - \frac{u}{r^2} \right), \tag{3.3}$$

$$\rho_{nf}(w_t + uw_r + ww_z) = -p_z - \mu_{nf}(\nabla^2 w). \tag{3.4}$$

The momentum equation's governing model

$$\rho \frac{\partial V}{\partial t} + \rho(V.\nabla)V = \nabla \cdot [-PI + K] + F, \tag{3.5}$$

$$\mathbf{K} = \mu(\nabla \mathbf{V} + (\nabla \mathbf{V})^T),\tag{3.6}$$

where $\rho_{nf}\,$ is density of the nanofluid, μ_{nf} is its viscosity, and P is the fluid's pressure.

Energy Equation

$$(\rho C_P)_{nf}(\partial_t + w\partial_z + u\partial_r)T = k_{nf}(\partial_{rr} + \partial_{zz})T. \tag{3.7}$$

The controlling heat transfer equation is:

$$d_z(\rho C_p) \left(\frac{\partial T}{\partial t}\right) + d_y \rho C_P u. \nabla T + \nabla \cdot q = d_z Q + q_0 + d_z Q_p + d_z Q_{vd}. \tag{3.8}$$

Heat transfer equation of the solid obstacle inside the fluid

$$d_{z}(\rho C_{p})\left(\frac{\partial T}{\partial t}\right) + d_{y}\rho C_{P}u.\nabla T + \nabla \cdot q = d_{z}Q + q_{0} + d_{z}Q_{ted},$$

$$q = -d_{z}k\nabla T.$$
(3.9)

Where $Q_{vd} = \tau \nabla u$ denotes the viscous dissipation heat source $\tau = -PI + K$,

 $q=-d_z k \nabla T$. Q denotes heat source ∇T denotes temperature gradient and d_z is the fluid's thickness.

Initial Values:

$$u = 0$$
 , $w = 0$, $T = T_0$, and $P = 0$. (3.10)

The thermophysical features of nanofluid is defined as:

$$\rho_{nf} = (1 - \phi)\rho_f + \phi \rho_p ,$$

$$\mu_{nf} = \mu_f (1 - \phi)^{-2.5} ,$$

$$(\rho C_P)_{nf} = (1 - \phi)(\rho C_P)_f + \phi(\rho c_p)_p ,$$

$$k_{nf} = k_f \left[\frac{k_p + 2k_f - 2\phi(k_f - k_p)}{k_p + 2k_f + \phi(k_f - k_p)} \right] .$$
(3.11)

Boundary Conditions

The boundary condition consists of inlet, outlet, wall and thermal.

The Inlet

The Newtonian fluid rate was estimated at the entrance of the 2D cylinders. The area of the inflow path and the intake velocity can be used to modify the fluid volume. The model's input is determined as illustrated in Fig. 3.3. Below is the inlet boundary condition:

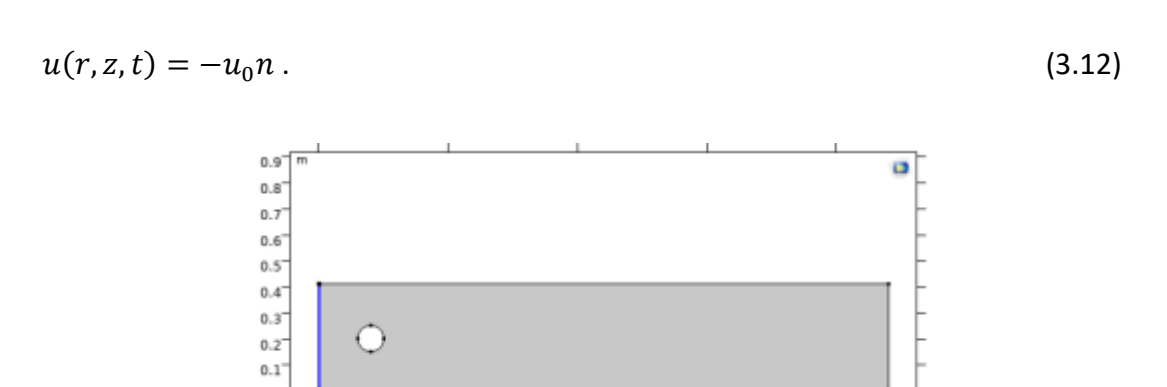


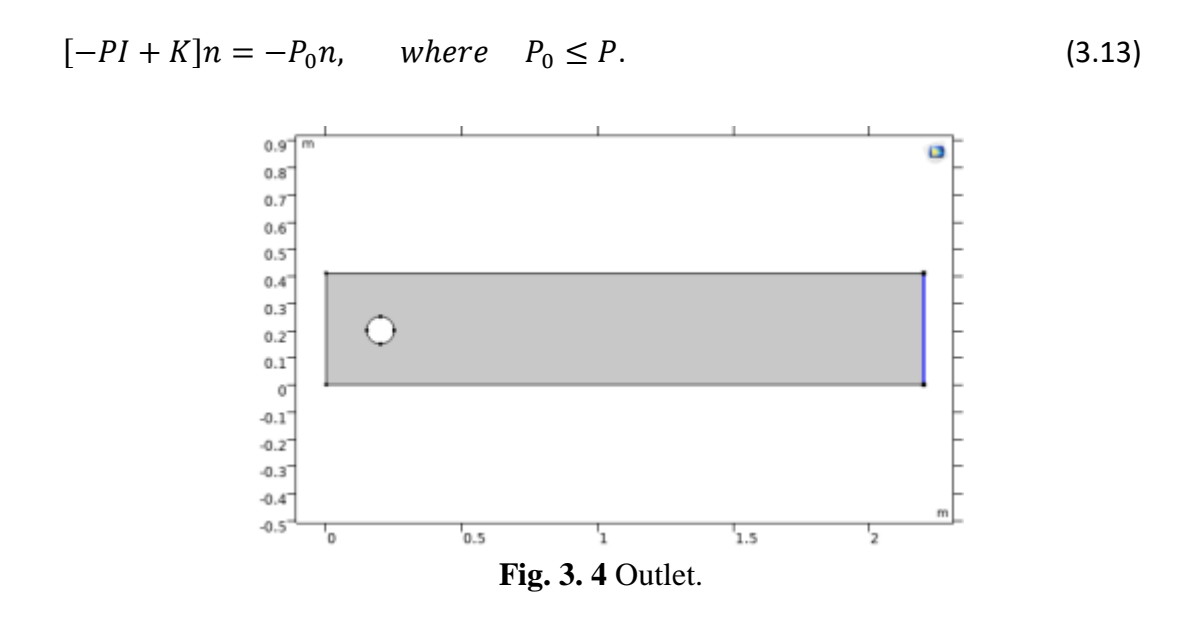
Fig. 3. 3 Inlet.

1.5

The Outlet

-0.3

The model incorporates pressure at the outflow to increase realism. The outlet that the fluid exited through is depicted in Fig. (3.4.) It was positioned across from the entrance.



At the Wall

-0.2°

Due to its viscosity, the Newtonian fluid under study is unable to pass through the wall and instead adheres to it. At the wall, the boundary and no-slip conditions were then measured. The 2D cylinder's walls are displayed in Fig. (3.5.)

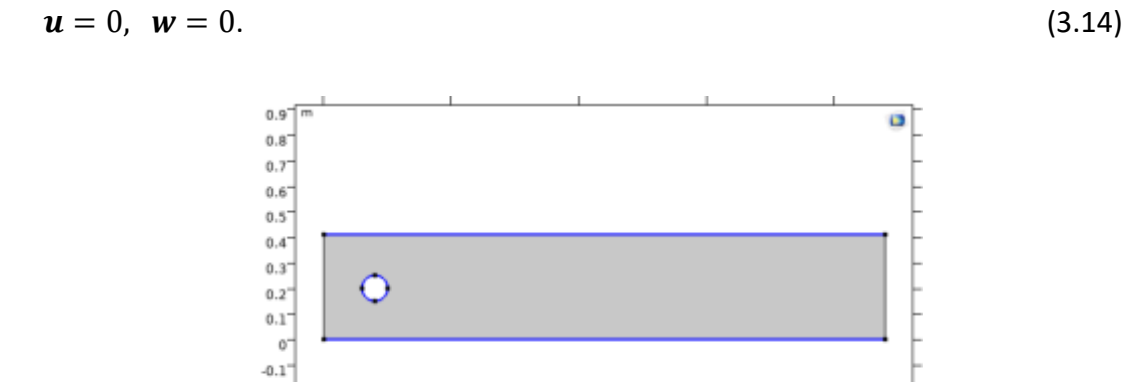


Fig. 3. 5 Velocity at wall.

Thermal Insulation

The insulating boundaries in COMSOL heat transfer module are shown in Fig. (3.6.)

Thermal insulation equation in COMSOL is:



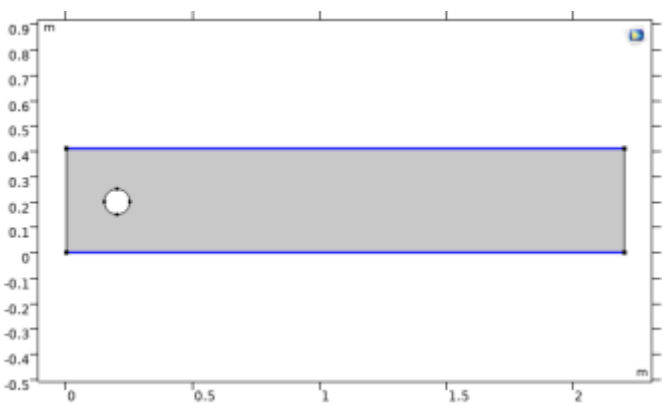


Fig. 3. 6 Thermal Insulation.

Temperature

Temperature at the inlet boundary in COMSOL Multiphysics are shown in Fig. (3. 7.) the temperature at inlet boundary is 300K.

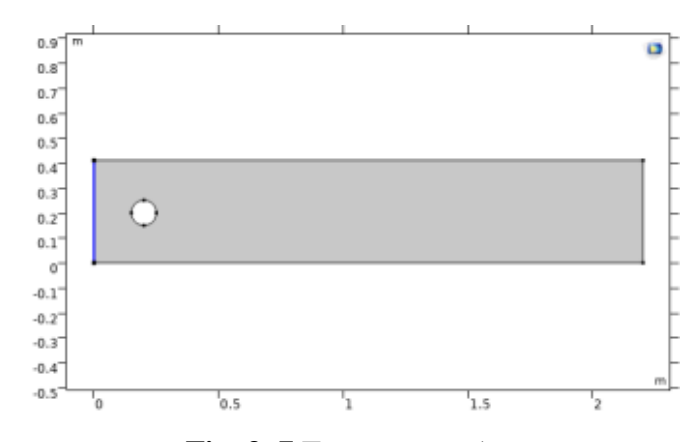


Fig. 3. 7 Temperature 1.

Temperature at the Surface of the Solid Obstacle

Temperature of solid obstacle was set to be 350K which is shown in Fig. (3. 8.)

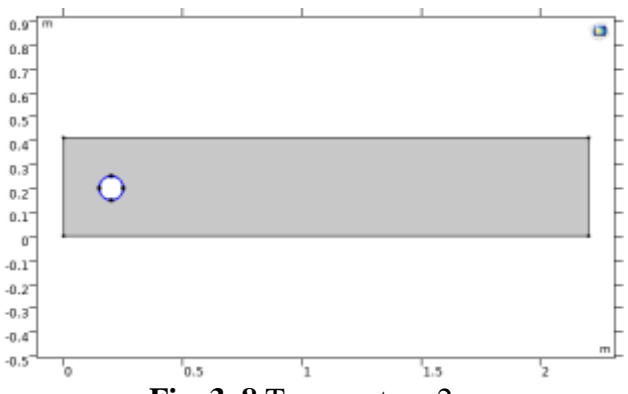
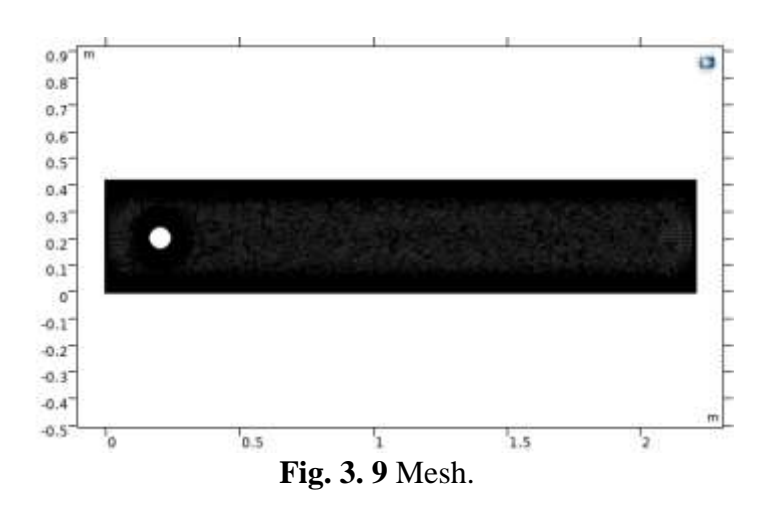


Fig. 3. 8 Temperature 2.

Computational Mesh

A mesh is an essential component of CFD, or computational fluid dynamics. The mesh quality affects the accuracy and convergence rate of the solution. COMSOL's 'physics driven mesh' is used to generate the mesh independently. The mesh of extra-fine elements is more accurate and performs better than standard mesh. A finer version of the element mesh is shown in Fig. (3. 9.)



Similarly for two solid obstacles all boundary conditions are same.

3.3 Results and Discussion

The results from two distinct geometrical configurations—one with a single solid obstacle and another with two solid obstacles positioned inside a 2D confined cylinders are shown and contrasted in this section. Under thermal boundary conditions, the study examines the effects of the placement and presence of these barriers on the nanofluid's convective flow and heat transfer properties. According to the simulation results, adding a solid obstacle dramatically changes the flow pattern by raising pressure close to the obstacle surface and strengthening the thermal boundary layer. Additional disruption is seen in the double-obstacles configuration, leading to more intricate flow separation and recirculation zones as well as faster heat transfer rates.

Both temperature distribution and velocity profiles are analyzed to understand the behavior of nanofluid flow across different regions of the domain. The influence of thermal conditions and nanoparticle interaction on flow resistance, pressure drop, and convective heat transfer is also discussed in detail.

Surface Velocity Magnitude for Single Solid Obstacle

This section addresses the fluid behavior and velocity variation of a nanofluid under thermal boundary conditions interacting with a single solid obstacle embedded in a 2D channel. In order to investigate the fluid dynamics and velocity distribution, the observations were captured at various points in time.

Fig. 3. 10 (a—f) illustrate values of the velocity profile for intervals 0.2, 2.8, 3.5, 4.8, 6.2, and 7 seconds.

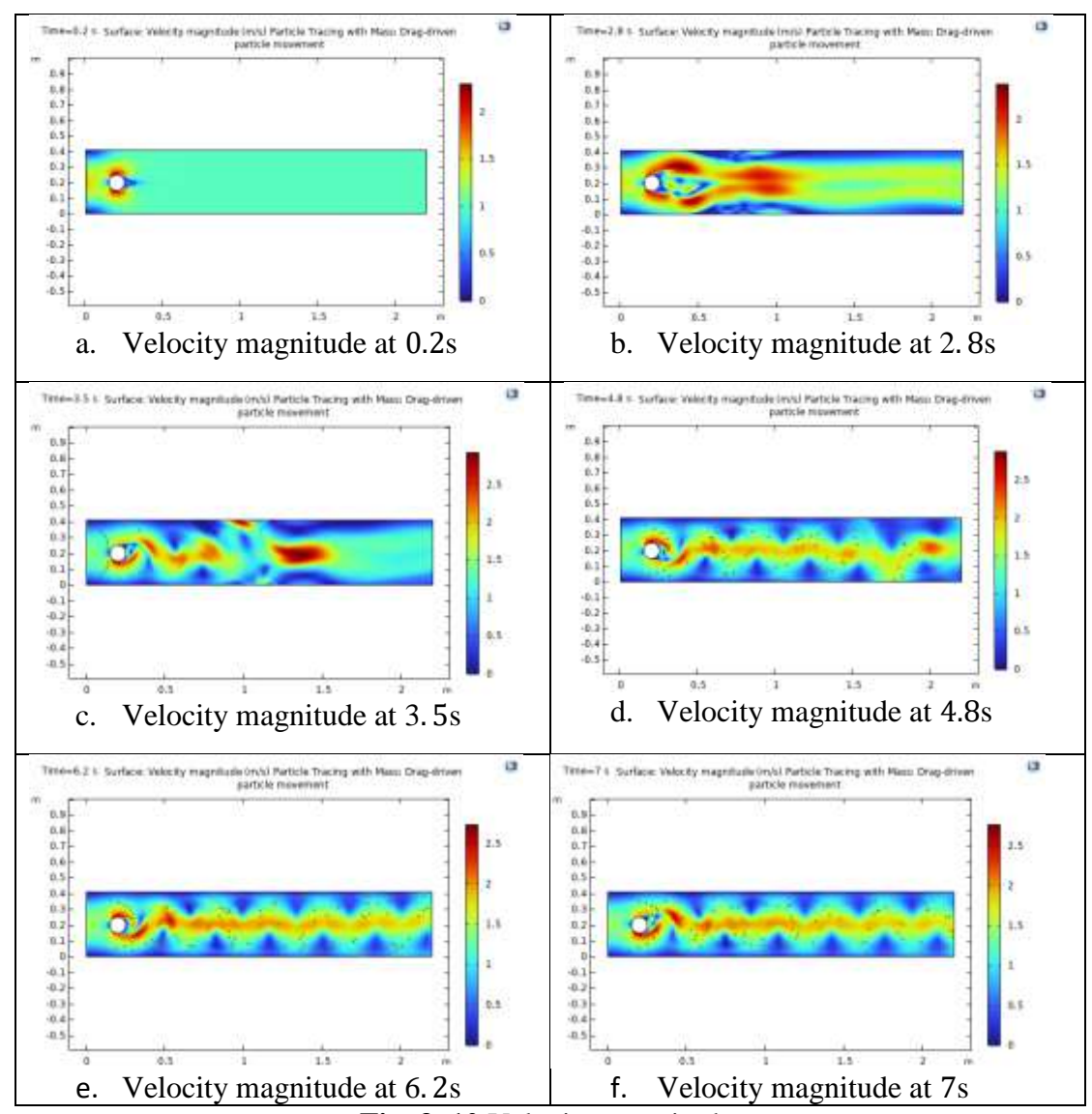


Fig. 3. 10 Velocity magnitude.

Fig. 3.10(a) When the nanofluid first enters the domain, it hits the cylindrical obstruction right away. The fluid starts to split along the top and bottom edges of the fragment as it gets closer to the solid obstacle front surface. The no-slip boundary condition causes the velocity at the cylinder's surface to almost zero, while flow constriction causes the velocity in the centerline to slightly increase. Just downstream of the obstacle, a peak velocity of roughly 2.5 m/s is seen, signifying the impact of contraction and fluid acceleration close to the center axis. Fig. 3.10(b) shows the fluid development of wake regions and vortex shedding downstream of the obstacle as the simulation goes on. Behind the obstacle, a wider area of high-speed flow (between 1.5

and 2.0 m/s) forms as the velocity field becomes more disrupted. The constant separation and reattachment of the flow, particularly at the wake boundary, suggests increased mixing and unsteadiness. Following the contraction effects, there are indications of recovery as the surface velocity near the outlet region becomes comparatively smoother.

Fig. 3.10(c) at 3.5 seconds, shows the vortex structures are more noticeable at this later stage, especially in the vicinity of the obstacle rear. With alternating zones of high and low velocity forming along the centerline and close to the obstacle wake, the nanofluid exhibits stronger circulation patterns. In areas where the fluid accelerates through constrained wake paths, a peak velocity of roughly 2.6 m/s is noted. These vortices cause mixing, which produces a more consistent velocity profile toward the outlet and reflects the steady-state trend that forms under conditions of continuous flow. Fig. 3.10(d) indicates at this point, a distinct wake structure is starting to form behind the obstacle as a result of the nanofluid's interaction with the cylindrical obstacle. The noslip condition keeps the velocity close to the front stagnation point low, but it is evident that flow separation happens along the obstacle curved edges. In the downstream area, high-velocity zones (near 2.5 m/s) appear, mostly along the centerline. With alternating areas of high and low speed following the obstacle, the velocity distribution exhibits the first indications of periodic vortex shedding. Curved particle paths reveal earlystage mixing and rotational flow behavior. Fig. 3.10(e) Behind the cylinder, more distinct and stable vortex streets form as the flow progresses. Clearer periodic patterns of alternating high and low velocities, which are indicative of the von Kármán vortex street, are seen in the nanofluid. Localized acceleration zones caused by wake contraction are highlighted by velocity magnitudes behind the solid obstacle, which reach about 2.6 m/s. Increased mixing and flow unsteadiness are indicated by the particle traces becoming more in line with the wake's oscillatory characteristics. The boundary layer behavior close to the obstacle is still influenced by thermal effects, which help to create the structured separation zones. Finally Fig. 3.10(f) shows The wake patterns exhibit more regularity in the flow field at this advanced simulation time, with the downstream region dominated by symmetric and periodic vortex structures. Peak velocities in the wake core once more approach 2.6 m/s, indicating the persistence of the alternating velocity bands. Strong recirculation zones result from the interaction of velocity shears and thermal gradients, especially close to the obstacle rear surface. In the far wake, the nanofluid particles show smoother trajectories, indicating a shift toward quasi-steady flow with efficient thermal transport and prolonged mixing.

Surface Velocity Magnitude for Double Solid Obstacles

The fluid behavior and velocity variation of a nanofluid interacting with two solid obstacles embedded in a 2D cylinder under thermal boundary conditions are covered in this section. Observations were made at various points in time to investigate the fluid dynamics and velocity distribution. Dual barriers result in more intricate flow separation and interaction, which affects the surface velocity and pressure distribution surrounding each obstacles.

Fig. 3. 11 (a—f) illustrate values of the velocity profile for intervals 0.2, 2.8, 3.5, 4.8, 6.2, and 7 seconds.

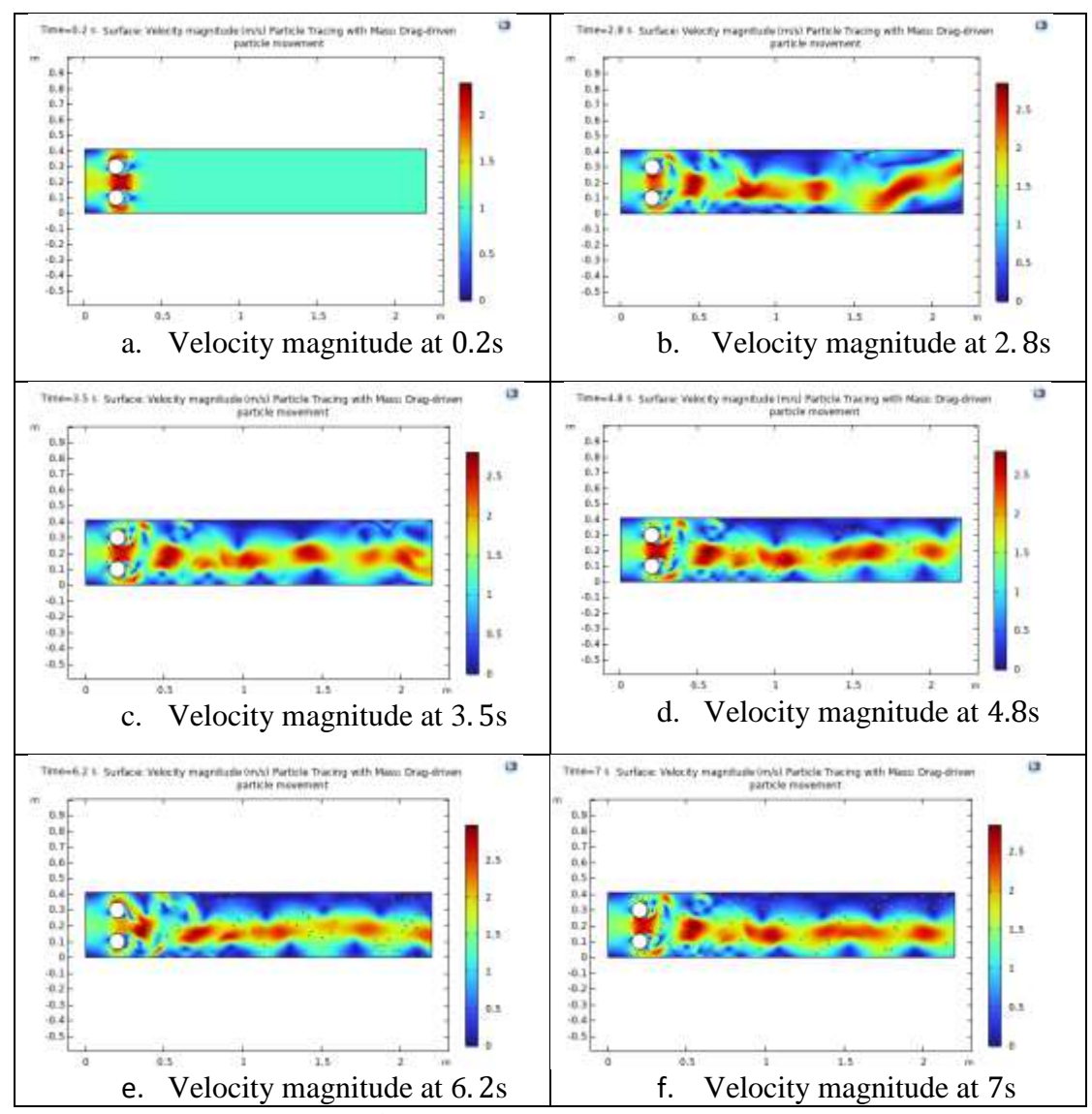


Fig. 3. 11 Velocity magnitude.

Fig.3.11(a) shows the velocity contour at 0.2s, representing the early stage of nanofluid flow over two solid obstacles. There is not much disturbance in the wake region at this time, and the flow is uniform and smooth. The formation of boundary layers causes a distinct velocity gradient to appear around the cylinder surfaces. The peak velocity, which is mostly concentrated close to the spaces between the obstacles where flow acceleration happens because of geometric constriction, reaches about 2.2 m/s. Fig 3.11(b) illustrates the velocity magnitude at 2.8s, Behind the obstacles, flow separation is now clearly visible, and vortex shedding starts to form. There are chaotic flow structures in the wake region as a result of thermal boundary effects and convection

enhanced by nanoparticles. Particularly close to the back of the lower obstacle, where vortices are more intense, velocity magnitudes exhibit localized peaks at about 2.5 m/s. Higher dispersion in nanoparticles indicates strong drag-driven movement that is influenced by temperature gradients. Fig 3.11(c) displays the velocity field at 3.5s, where patterns of swirling vortices become more noticeable behind and between the obstacles. These patterns show that unstable vortex streets are forming. Stronger recirculation zones are a result of the interaction between the thermal boundary and nanofluid characteristics. Nanoparticles are clearly dispersed along the vortex edges, indicating improved mixing, and the velocity increases marginally at specific locations, reaching up to 2.6 m/s. The velocity profile at 4.8s, when the flow has grown more unstable, is shown in Fig. 3.11(d). Downstream, a number of vortex structures form intricate wake interactions. While velocities near the obstacle walls fall below 1.0 m/s, indicating strong shear and energy dissipation as a result of thermal and nanoparticle interaction, the highest velocity magnitude observed is approximately 2.7 m/s near the lower wake core. It can be deduced from Fig. 3.11(e) at 6.2s, that the vortex shedding becomes more regular and that the spread of nanoparticles keeps improving thermal mixing across the domain. The flow at 7s, is shown in Fig. 3.11(f), which shows a developed periodic shedding regime. Nanoparticles can be seen tracing the highvelocity areas along the wake as the nanofluid now completely fills the domain. There are noticeable stretches of fast-moving water downstream, and the maximum velocity stays near 2.6 m/s. Particles are more widely distributed and travel intricate routes that are impacted by thermal buoyancy as well as hydrodynamic forces.

Velocity Distribution (single solid Obstacle) for Horizontal and Vertical Directions:

Fig. 3.12(a—f) displays the horizontal velocity profile (x-axis) at times 0.2s, 2.8s, 3.5s, 4.8s, 6.2s and 7s.

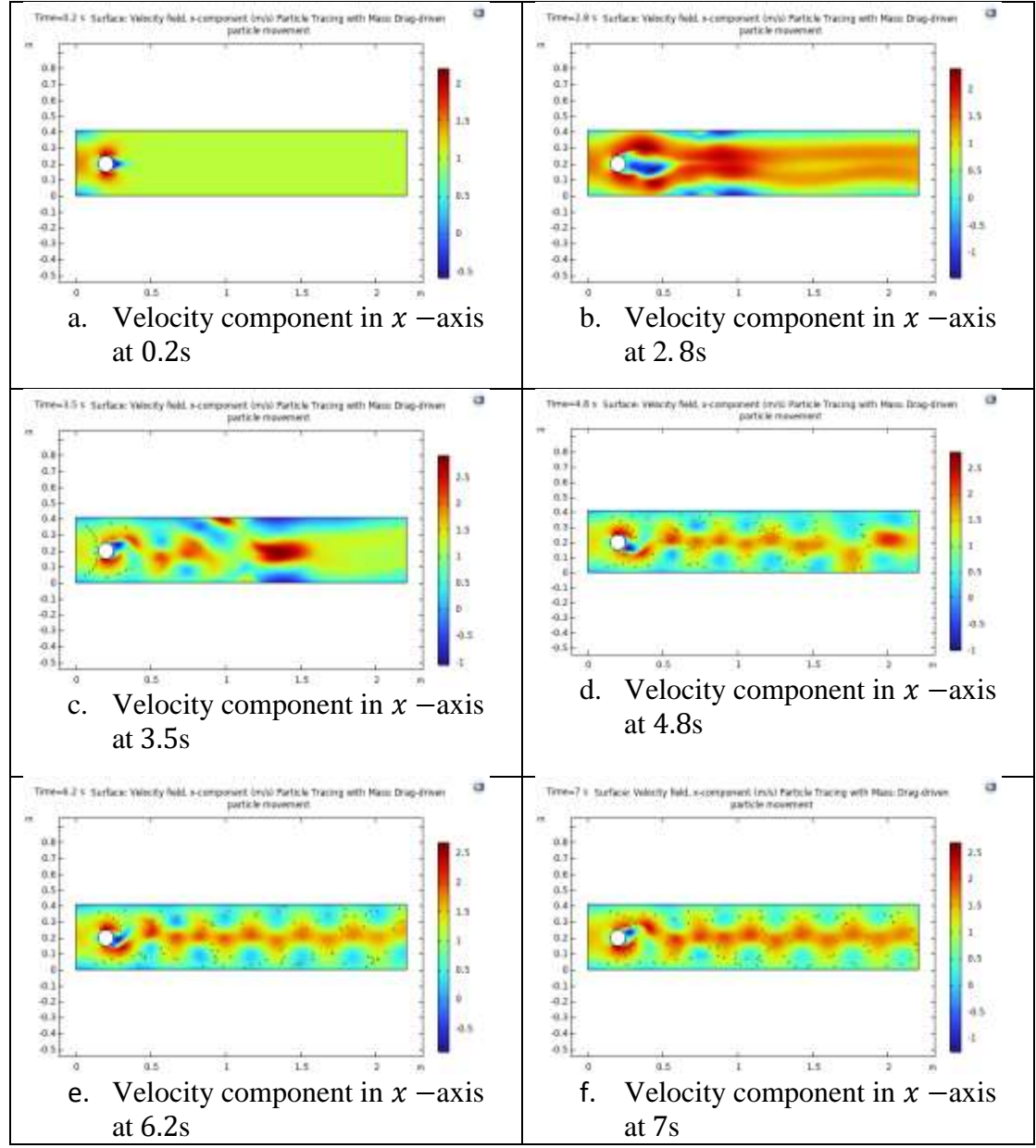


Fig. 3.12 Velocity profile at x-axis.

And surface velocity profile along the vertical plane (y - axis) are shown on fig. 3.13(a-f) at times 0.2s, 2.8s, 3.5s,4.8s,6.2, and 7s respectively.

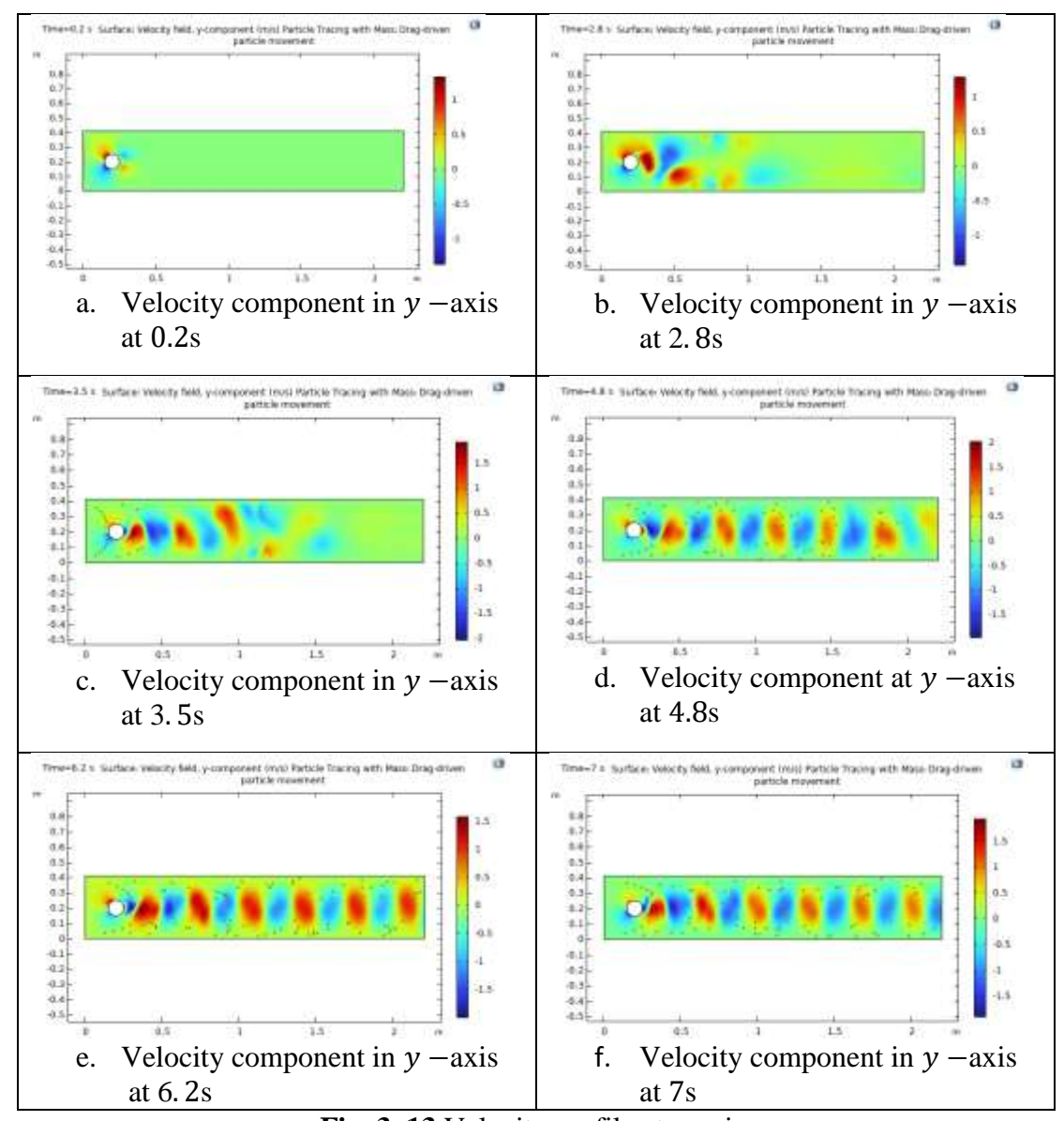


Fig. 3. 13 Velocity profile at y-axis.

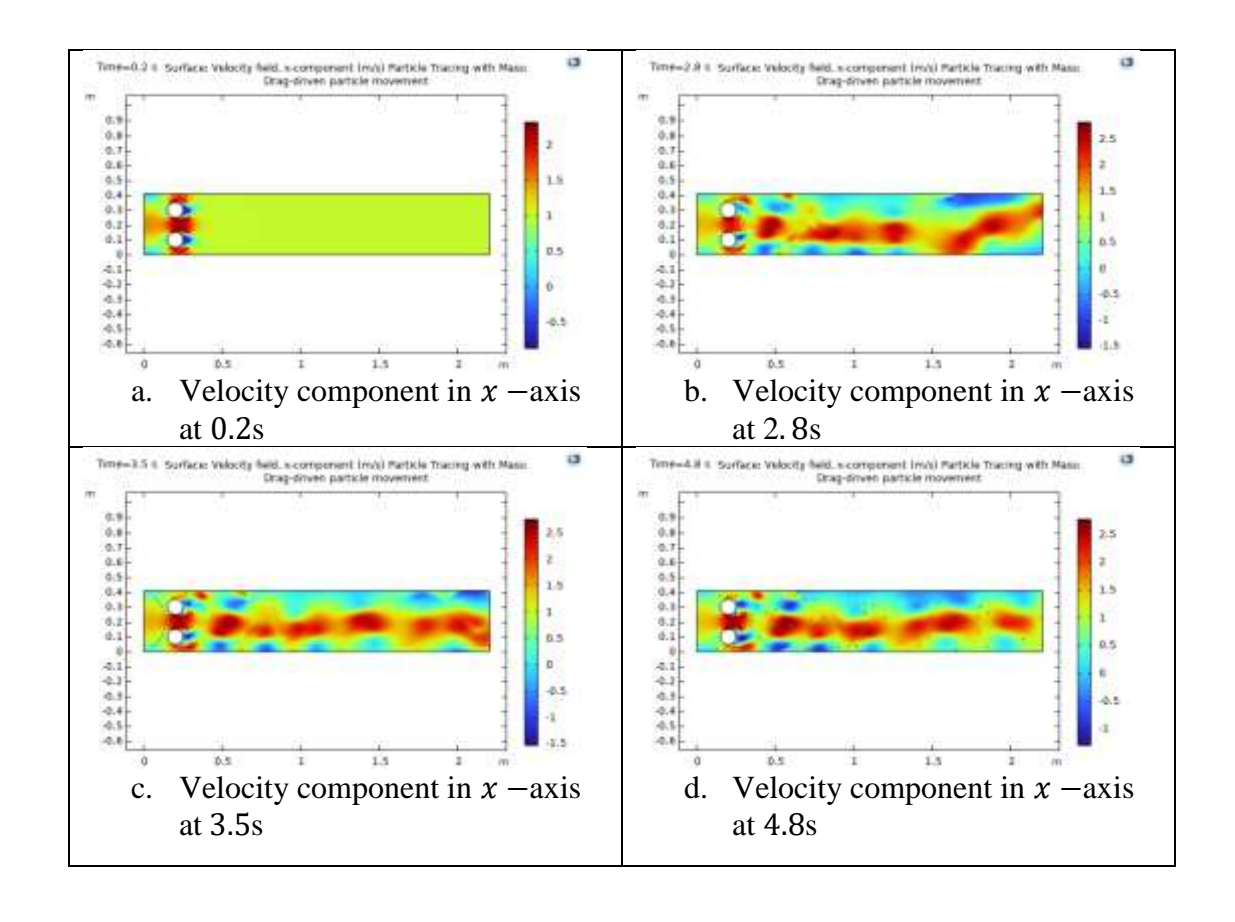
Fig.3.12(a) shows the flow has a nearly constant streamwise velocity of roughly 2.2 m/s as it approaches the obstacle. While flow separation has not yet fully developed, the centerline velocity slightly accelerates as a result of contraction around the cylindrical obstacle. Fig3.12(b) shows the pressure drop behind the obstacle causes acceleration in the wake. At the centerline, peak x-velocity rises to 2.4 m/s. Recirculation starts close to the wall regions, while streamwise momentum transport is improved by the thermal response of the nanofluid. Significant spatial variations in velocity are caused by stronger wake formation at t=3.5 s. There are low-speed recirculation zones and high-speed jets. The top speed is 2.5 m/s. The nanoparticles speed up flow downstream and

alter viscosity locally by increasing heat conduction. Behind the cylinder, a fully formed wake appears at t = 4.8 s. Vortex shedding seen in the y-component is consistent with alternating zones of fast and slow x-velocity. While decelerated zones form near the obstacle edges, the main flow's velocity stays high at about 2.4 to 2.5 m/s. The steady vortex street in the y-direction corresponds to the streamwise flow becoming periodic at t = 6.2 s. The velocity streaks in the downstream flow are uniformly spaced. Nanoparticles improve thermal diffusion, which somewhat stabilizes the flow. A uniformly distributed velocity field is still present at t = 7.0 s. Near 2.5 m/s, the peak xdirection velocity stays constant. With few disruptions in the downstream jet, the flow around the obstacle has stabilized into a quasi-periodic state. Similarly the impact of contraction on nanofluid movement along the y-direction is depicted in Fig. 3.13(a-f). Fig.3.13(a) shows the flow is in its early stages of development at t = 0.2 s. Around the obstacle, the y-velocity is symmetrical, with maximum values located just downstream at about ±1 m/s. The formation of vortices has not yet begun. At this point, thermal boundary effects and nanoparticle influence are negligible. Behind the obstacle, vortex shedding starts at t = 2.8 s. A von Kármán vortex street is in its early stages when there are alternating high positive and negative velocities. Thermal gradients encourage fluid motion in a vertical direction, while nanoparticles increase flow instability. The surface velocity is around ± 1.4 m/s. Completely formed unsteady wake forms with alternating bands of vortices were observed at t = 3.5 s. The y-velocity reaches a maximum of about ±1.8 m/s. As thermal gradients promote increased vertical motion and nanoparticles amplify the unsteadiness, the flow becomes asymmetric. Shear layers start to separate more quickly. A more robust and distinct vortex street begins to form at t = 4.8 s. The oscillation of a vertical fluid becomes periodic. Better mixing results from the ongoing enhancement of chaotic lateral velocity behavior caused by

nanoparticles. The y-direction velocity peaks at about ± 2 m/s. The flow settles into a periodic shedding pattern with wider wakes at t=6.2 s. Extreme velocity fluctuations are somewhat attenuated by the viscosity of the nanofluid, but the vortex shedding is maintained by the thermal effects. In the wake, the vortices are now more evenly spaced. At t=7.0 s, the y-direction is dominated by stable, periodic vortex structures. The maximum speed is kept at about ± 2 m/s. An enlarged oscillatory wake is a result of the thermal boundary condition's buoyancy effects and nanoparticle drag, which have a substantial impact on the flow structure.

Velocity Distribution (double solid Obstacles) for Horizontal and Vertical Directions

Fig. 3.14(a—f) displays the horizontal velocity profile (x-axis) at times 0.2s, 2.8s, 3.5s, 4.8s, 6.2s and 7s.



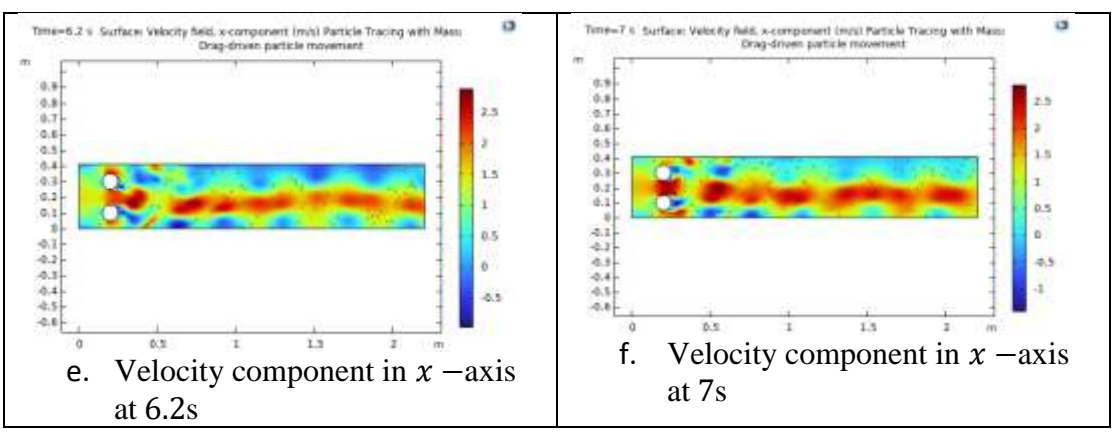
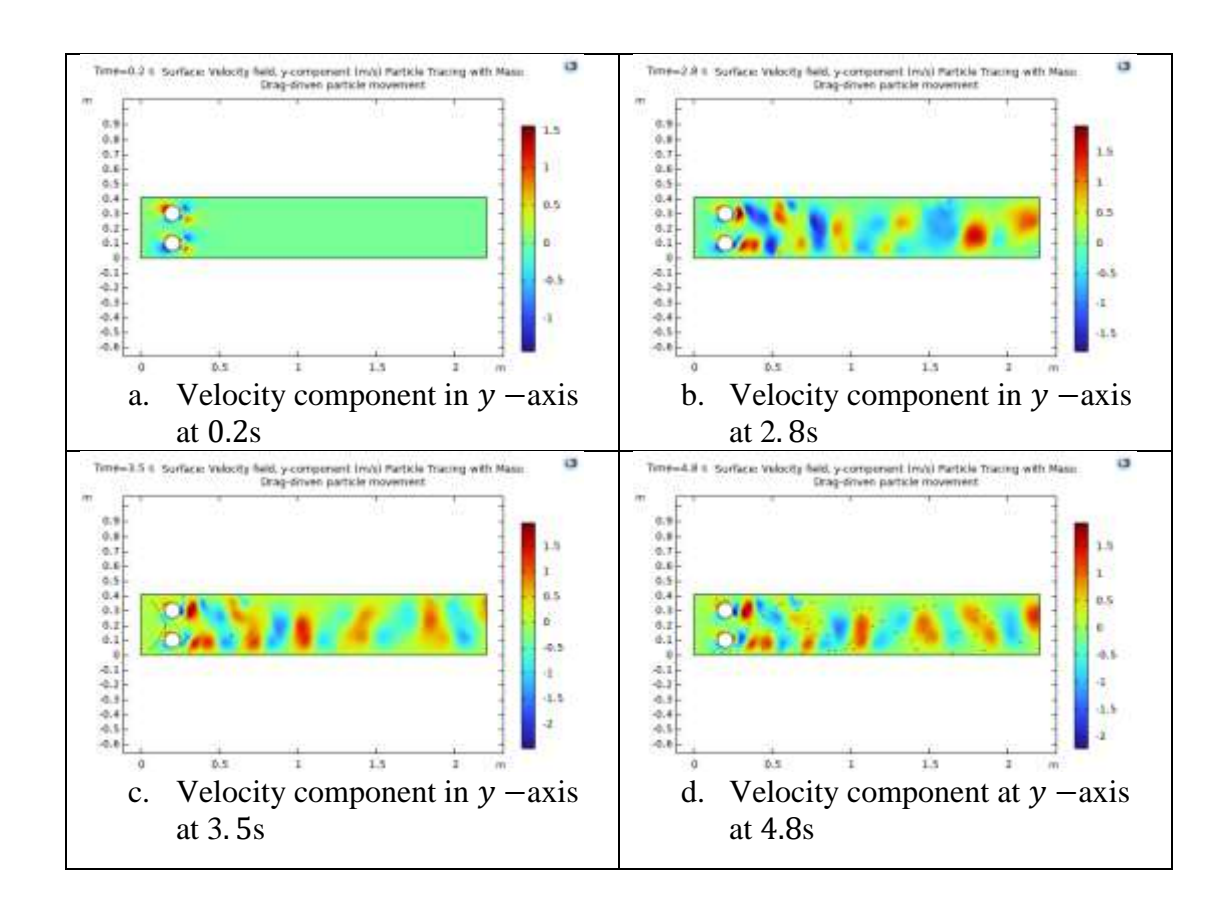


Fig. 3.14 Velocity profile at x-axis.

And surface velocity profile along the vertical plane (y - axis) are shown on fig. 3.15(a—f) at times 0.2s, 2.8s, 3.5s,4.8s,6.2, and 7s respectively.



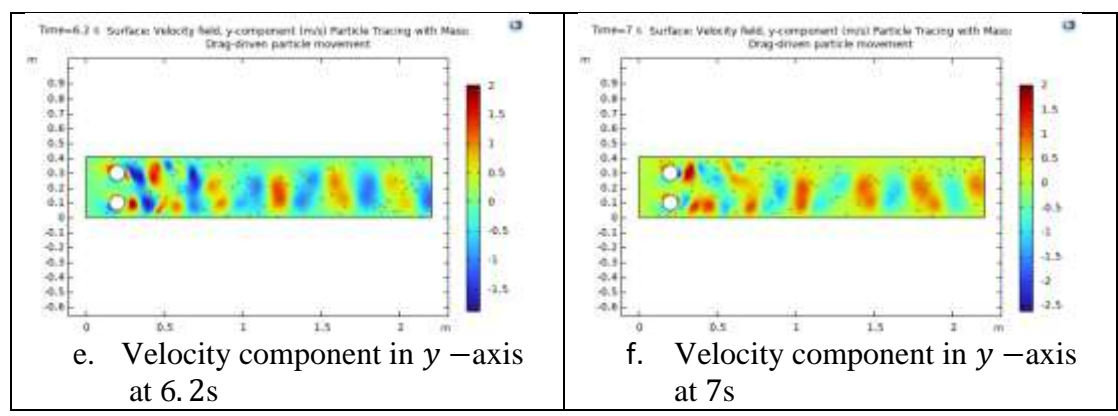


Fig. 3. 15 Velocity profile at y-axis.

The evolution of the x-component of velocity for a nanofluid passing two solid obstacles obstructions positioned inside a confined cylinder over time (from 0.2 s to 7 s) is shown in Fig. 3.14(a-f). In addition to the momentum exchange caused by suspended nanoparticles, the presence of the solid obstacles and thermal boundary conditions also affect the velocity field. Fig.3.14(a) shows when the nanofluid first enters the domain, the velocity field starts to form. Behind the obstacles, the streamwise velocity reaches about 2.0–2.2 m/s. The early formation of boundary layers is suggested by the symmetric disturbance pattern close to the obstacles. The influence of suspended nanoparticles and low Reynolds number effects result in little flow separation and comparatively aligned streamlines. The flow structure has not yet been substantially changed by the thermal boundary effect, which is only now starting to take shape. The flow downstream of the cylinders becomes increasingly erratic by 2.8 seconds. Vortex shedding behind each cylinder causes pockets of high and low velocity, demonstrating interaction between the shear layers. The streamwise velocity exhibits jet-like acceleration and localized flow reversal, varying between -1.5 m/s and 2.5 m/s. The overall mixing of the nanofluid is increased and convection effects are amplified by the thermal gradient. Particularly close to the upper and lower boundaries, wake regions enlarge and velocity perturbations become more apparent. Fig. 3.14(c) behind both obstacles, a distinct vortex street is seen, and the flow asymmetry increases. Alternating

acceleration and deceleration zones that are in line with vortex cores can be seen in the velocity profile in the x-direction. While reverse flow pockets (shown in blue) indicate recirculation zones close to the walls, the peak x-velocity stays at about 2.5 m/s. This behavior is typical of von Kármán vortex shedding, which is now more impacted by the drag and buoyancy caused by thermally induced nanoparticles. Compared to singleobstacle configurations, the interaction of the vortices from double obstacles results in more intricate patterns. Fig. 3.14(d). shows the velocity field appears wider and more diffused downstream, and the wake gets more turbulent. Now that the nanoparticles are widely dispersed, there is more drag and momentum exchange. Particle-fluid interaction causes energy dissipation, which results in a slight decrease in peak xvelocity values. However, along the centerline, jet-like flows continue to exist. Periodic vortex shedding and downstream transport are indicated by the distance between highvelocity streaks. Figure 3.14(e) shows a periodic structure starts to form in the surface velocity field. Dominant high-velocity zones, particularly behind the lower obstacle, are suggested by consistent red and yellow streaks in the midstream region. The maximum x-velocity stays at about 2.5 m/s due to some flow structure merging caused by the interaction between the two obstacle wakes. However, because of the no-slip condition and drag-induced dissipation from thermal boundary effects, the near-wall regions continue to be slower. When the flow reaches a quasi-periodic state, streamwise velocity maintains a steady but dynamic pattern, as seen in Fig. 3.14(f). Lower-speed zones alternate with high-speed jets, suggesting the development of an unsteady wake over time. The amplitude and distribution of velocity are both affected by the nanoparticles' complete integration into the flow. The velocity field is still affected by thermal buoyancy, especially close to the obstacle surfaces where temperature gradients are the steepest. Although the downstream vortices are more developed and widely separated, the flow's structure is still mainly consistent with earlier snapshots. Similarly Fig. 3.15(a) shows there is not much initial vertical movement. Because of obstruction, disturbances develop around the top and bottom of the cylinders. Y-velocity is primarily within ± 0.5 m/s, indicating that flow interacts with both obstacles early. Fig. 3.15(b) the wake behind both obstacles becomes asymmetric with vortex roll-up. Y-velocity reaches ± 1.2 m/s, indicating beginning of von Kármán vortex street. Upward and downward flow between and behind the cylinders grows stronger. Fig. 3.15(c) displays the y-direction exhibits a regular oscillation. Strong lateral flow is indicated by patterns that alternate between blue and red. Vertical momentum transfer and unsteadiness are improved by nanoparticle motion.

Fig. 3.15(d) and (e) at 4.8 and 6.2 seconds shows the upper and lower surfaces of both obstacles alternately develop and shed distinct vortex structures. At ~±1.8 m/s, the Y-velocity magnitude increases. Both thermal effects and particle-fluid interaction are responsible for this increased vertical mixing. Behind the obstacles in Fig. 3.15(f), the flow displays a developed and recurring vortex street. Regularly spaced vortices and dynamic equilibrium of vertical movement maintain mixing and recirculation.

Pressure Profile for Single Solid Obstacle

Figure 3.16 (a—f) shows the applied pressure distribution of Newtonian nanofluid flow around the circular obstacle at various time intervals: 0.2, 2.8, 3.5, 4.8, 6.2, and 7 seconds. This illustrates the progressive development of the pressure gradient and vortex shedding across the domain.

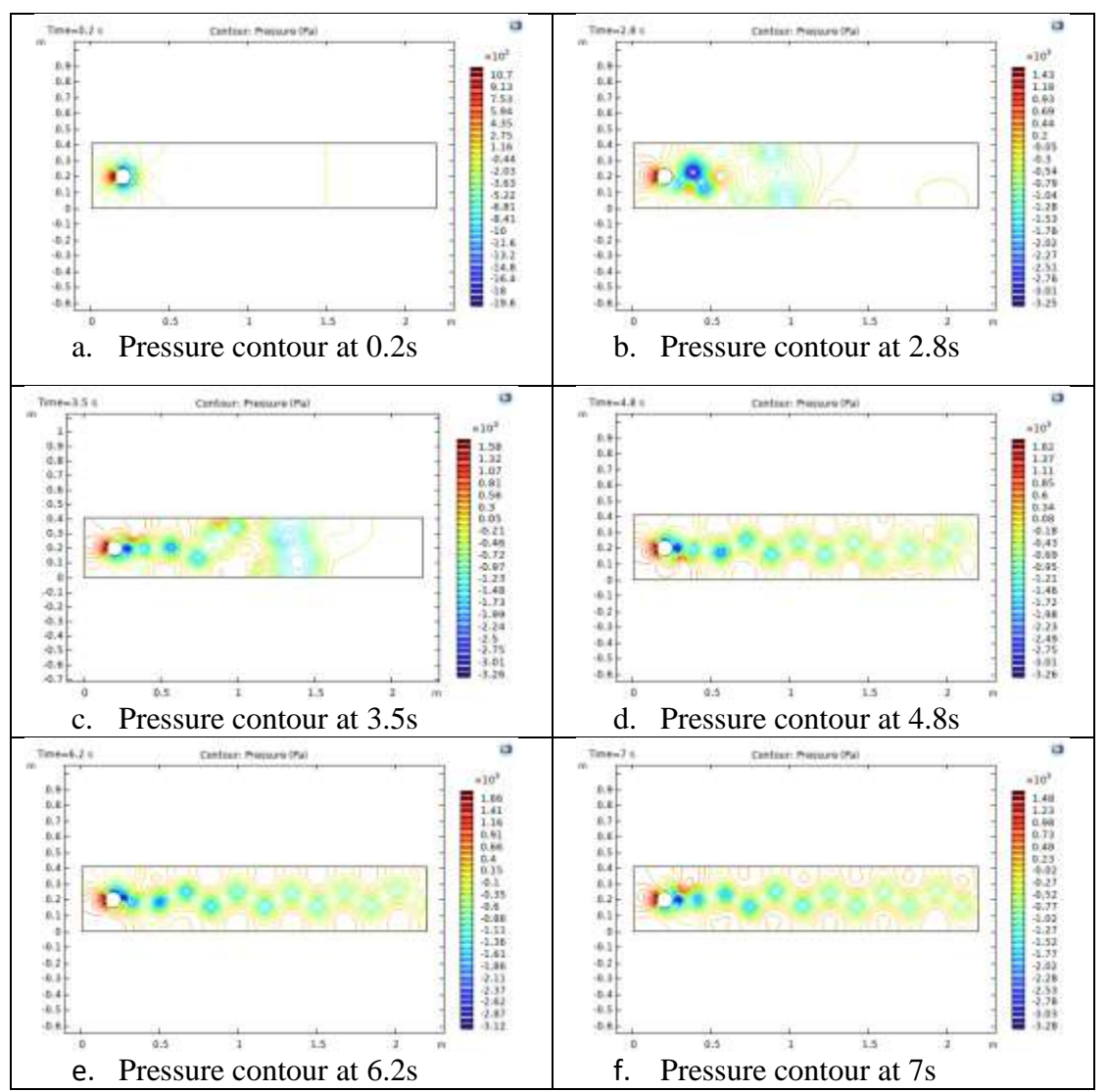


Fig. 3. 16 Pressure contour.

Fig. 3.16 (a) shows the pressure that the obstacle wall experiences as a result of the nanofluid's motion. The nanofluid flow has only just started to interact with the cylindrical obstruction at this early stage. At the obstacle front stagnation point, the pressure noticeably rises, reaching values as high as 1070 Pa. The fluid's direct impact on the front surface is what causes this. In the meantime, the pressure dramatically decreases behind and at the obstacle sides as flow separation begins, creating low-pressure zones. The pressure distribution becomes increasingly complicated, as Fig. 3.16 (b) illustrates. The development of vortex structures is indicated by the flow starting to separate from the obstacle surface and creating alternating low- and high-pressure areas behind it. While the upstream region maintains a high-pressure zone, a

steep pressure drop is seen behind the obstacle, reaching about -3250 Pa. The early phases of a vortex shedding process are indicated by these patterns. Fig. 3.16(c) shows that the vortex shedding process becomes more firmly established by t = 3.5 s. Clearly visible downstream of the obstacle are alternating pressure contours that display a Von Kármán vortex street. As vortices are released from either side of the obstacle, the pressure profile shows recurring peaks and valleys. There is a minimum pressure of about -3260 Pa and a maximum pressure of about 1580 Pa. As improved thermal conductivity helps to slightly stabilize vortex spacing, the impact of the nanofluid increases. The vortex structures are completely formed and evenly spaced throughout the downstream area in Fig. 3.16 (d). There are distinct contour lines and periodic behavior in the pressure profile. Although the values show a more consistent spatial frequency, they still fall within a similar range. This implies that a quasi-steady periodic shedding regime has been entered by the flow. The pressure profile still exhibits regular oscillations in the downstream wake region at t = 6.2 s, as seen in Fig. 3.16(e). More compact and well-defined vortices result from the interaction of thermal boundary conditions and nanofluid motion. The front's high-pressure area stays steady, and the wake's lowest pressure areas line up with vortex cores, suggesting that swirling flow facilitates effective energy exchange. Finally, a well-established flow pattern with symmetric and stable vortex shedding is shown in Fig. 3.16 (f). The pressure exhibits persistently high gradients, peaking at 1480 Pa and falling as low as -3280 Pa. The constant creation and movement of pressure waves along the channel suggests that the Newtonian nanofluid's interaction with the thermal wall boundary amplifies convective effects.

Pressure Profile for Double Solid Obstacles

The evolution of vortex shedding, pressure variation, and interaction between the wakes of the two obstacles are clearly demonstrated by the applied pressure distribution of Newtonian nanofluid flow around the double circular obstacles, which is depicted in Fig. 3.17(a—f) at various time intervals: 0.2, 2.8, 3.5, 4.8, 6.2, and 7 seconds.

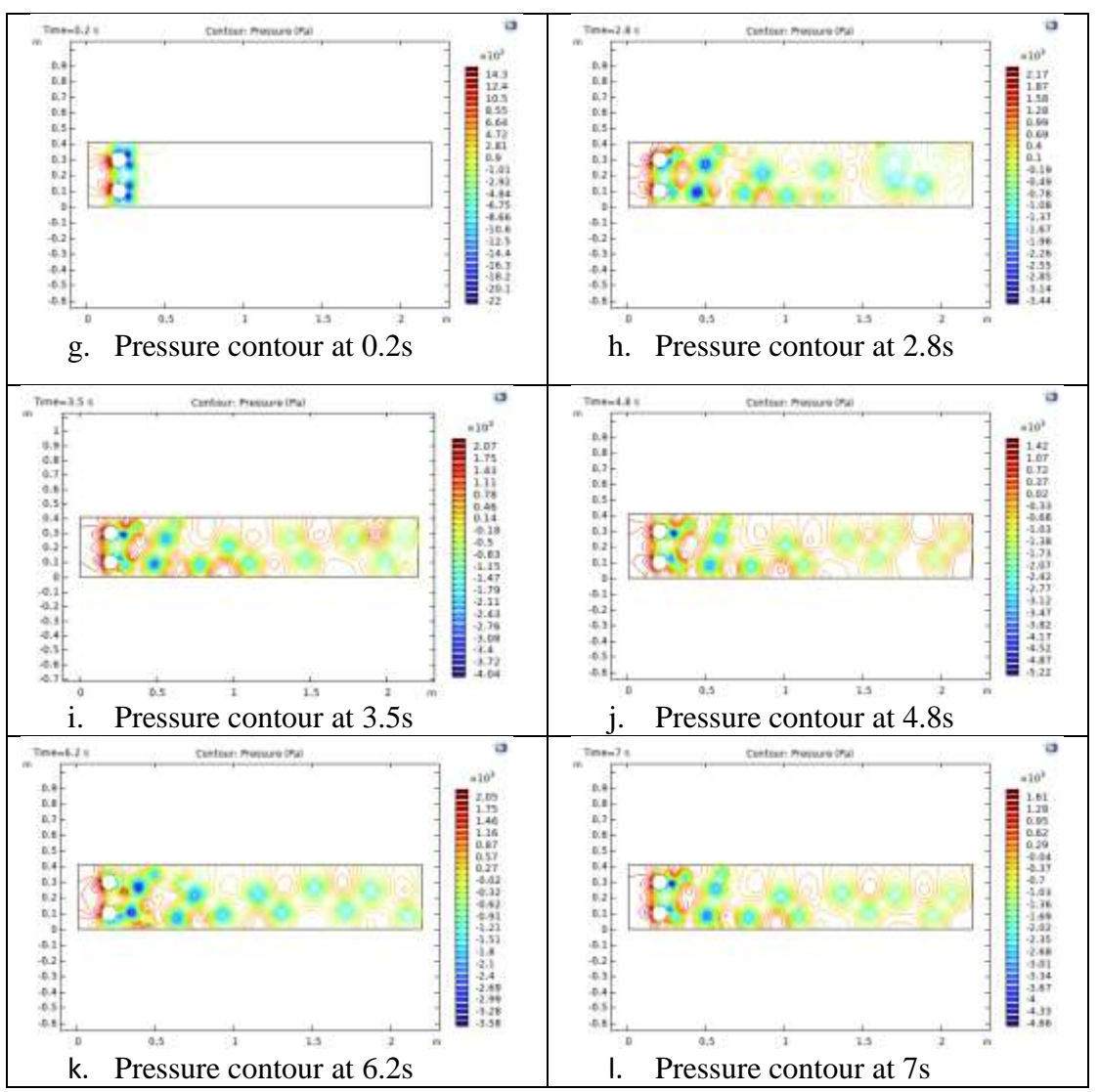


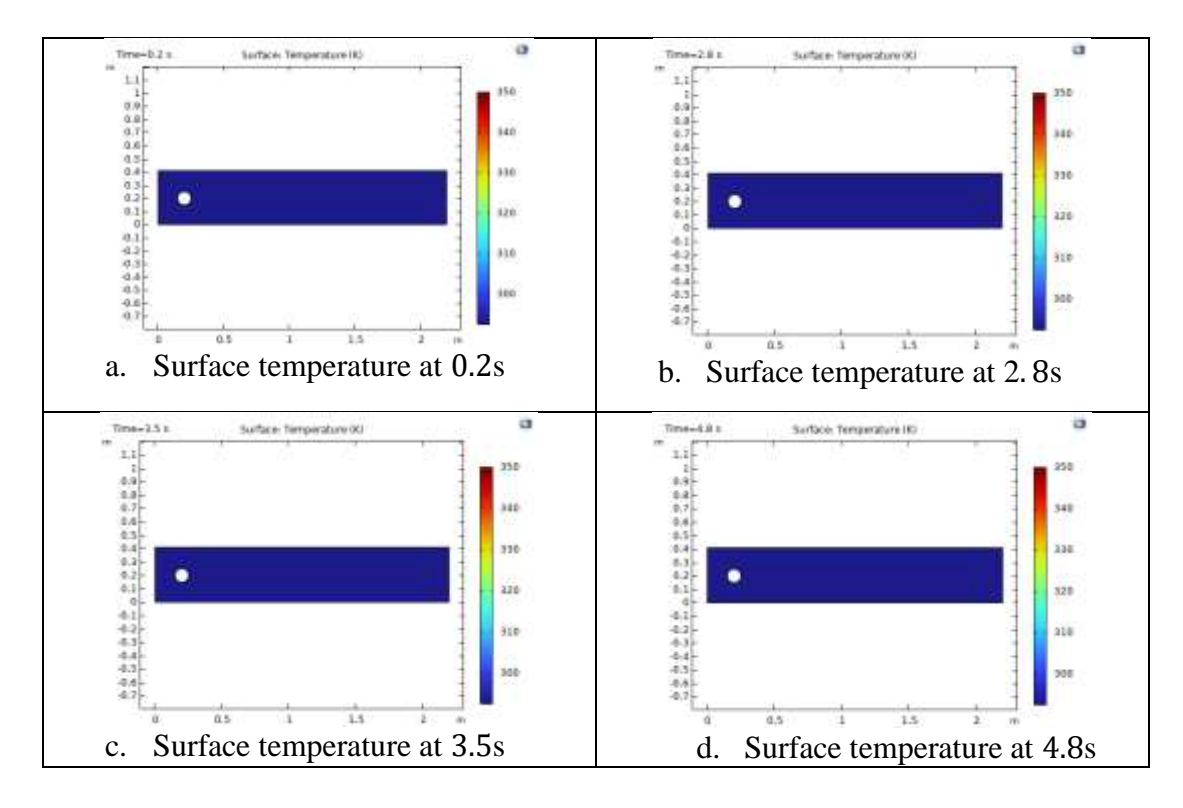
Fig. 3. 17 Pressure contour.

As seen in Fig. 3.17(a), the flow starts interacting with the front obstacles at the beginning of the simulation. Significant low-pressure regions of up to -22×10² Pa start to form behind the obstacles as a result of early flow separation, while the high-pressure regions are clearly visible on the cylinders' front faces, with values reaching up to

+14.3×10² Pa. At this point, the pressure contours are symmetrical, suggesting laminar and steady flow characteristics. Pressure gradients rise when there are several cylinders present because of the intricate interactions between boundary layers. Fig. 3.17(b) shows in the wake of the obstacles, vortex formation is visible at this time step. With alternating zones of high and low pressure in the downstream region, the pressure distribution has become increasingly erratic. The pressure reaches a minimum of -3.44×10³ Pa and a maximum of approximately +2.17×10³ Pa. This indicates the beginning of unsteady flow and vortex shedding. The interference between nearby wakes causes the flow between the obstacles to become more disturbed and gives rise to secondary flow structures. The downstream vortex street becomes more distinct and periodic, as seen in Fig. 3.17(c). High and low areas alternate in pressure contours, indicating the formation of a Von Kármán vortex street. The lowest pressure is - 4.04×10^3 Pa, and the highest pressure is still over $+2.07\times10^3$ Pa. This stage denotes increased fluid motion caused by the interaction of viscous and inertia forces. The increased momentum diffusion caused by the nanofluid's higher thermal conductivity could also affect wake stabilization. At this point, the flow field stabilizes into a repeating vortex shedding pattern, as seen in Fig. 3.17(d). The wake's pressure profile displays constant contour spacing, but the area close to the obstacles still exhibits pressure concentration because of continuous separation and reattachment zones. The downstream structure is shaped by the increasingly important influence of the rear obstacles. Stronger pressure fluctuations are indicated by the lowest value, which falls to about -5.22×10^3 Pa, and the highest value, which reaches roughly $+1.42 \times 10^3$ Pa. As the system enters a quasi-periodic shedding state, a more stable wake structure can be seen in Fig. 3.17(e). With a peak pressure of approximately +2.05×10³ Pa and a minimum pressure of approximately -3.58×10³ Pa, the pressure values are still within the same ranges as before. Nanofluid dynamics is partially responsible for the enhanced convective momentum transfer shown by the swirling flow downstream. Because of Bernoulli's principle, the flow close to the wall boundaries exhibits lower pressure zones, indicating maximum velocity. In Fig. 3.17(f), the pressure contours display a fully formed and structured vortex shedding pattern at this last recorded interval. The pressure reflects persistent high-pressure gradients, ranging from +1.61×10³ Pa to -4.66×10³ Pa. Downstream, the periodic vortex formation persists, suggesting a completely unstable but stable shedding regime. In engineering applications like heat exchangers and fluid transport systems, the nanofluid's continued promotion of improved mixing and thermal transfer can be advantageous.

Surface Temperature for Single Solid Obstacle

The surface temperature for single solid obstacle of the flow is shown in fig. 3.18(a—f) at 0.2, 2.8, 3.5, 4.8, 6.2, and 7 seconds respectively.



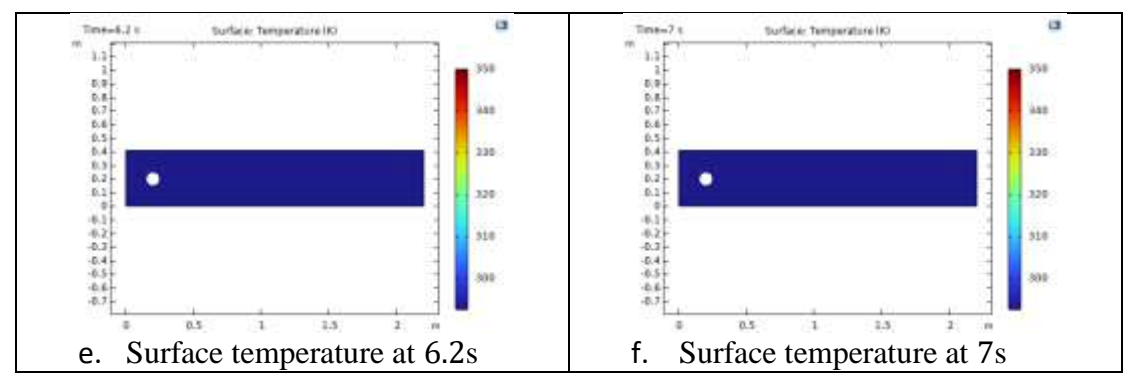


Fig. 3. 18 Surface temperature.

The inlet flow kept the temperature at 300 K, but the surface of the heated circular obstacle showed the highest temperature because of the applied thermal boundary of 350 K. The temperature near the upper and lower boundaries of the domain gradually rose from about 300 K to 305 K over time, as seen in Fig. 3.18(a,b,c,d,e,f). With surface temperatures rising to a maximum of 350 K, the area directly surrounding the obstacle exhibits constant thermal growth. Heat transfer was primarily concentrated close to the obstacle surface and wake region, as evidenced by the far field's ambient temperature staying closer to the inlet condition.

Surface Temperature for Double Solid Obstacles

The surface temperature for double solid obstacle of the flow is shown in fig. 3.19(a—f) at 0.2, 2.8, 3.5, 4.8, 6.2, and 7 seconds respectively.

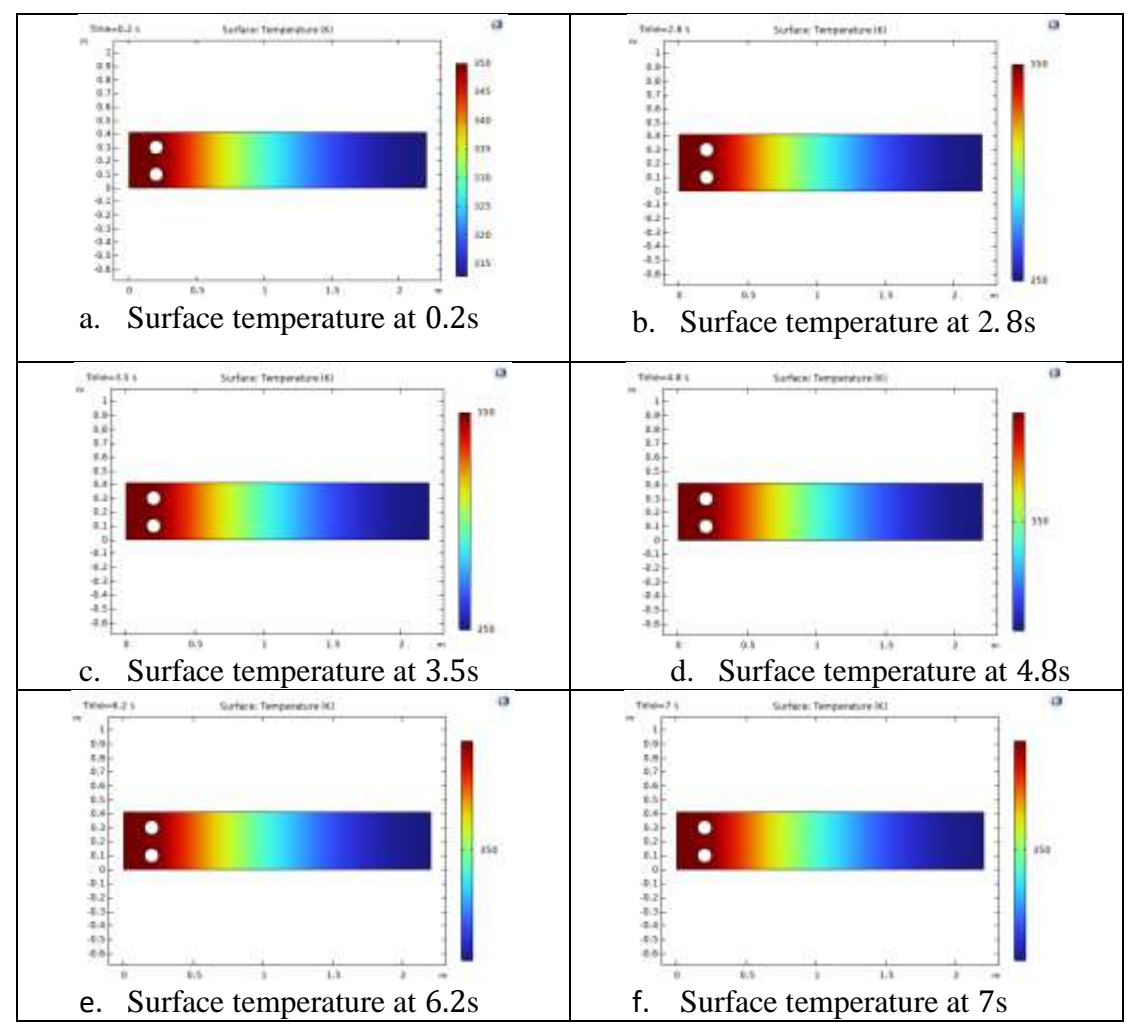


Fig. 3. 19 Surface temperature.

For the two solid obstacles, Fig. 3.19(a—f) shows the surface temperature distribution of Newtonian nanofluid flow at various time intervals: 0.2, 2.8, 3.5, 4.8, 6.2, and 7 seconds. A steady temperature gradient throughout the domain is produced by a fixed inlet temperature of 300 K and a constant solid wall temperature of 350 K. A distinct thermal boundary layer is created as the fluid gradually absorbs heat from the heated obstacles walls. Stable thermal diffusion downstream is indicated by the lowest temperature near the outlet remaining close to 313 K and the highest temperature near the obstacles surfaces remaining around 350 K.

Lift Coefficient Graph for Single Solid Obstacle

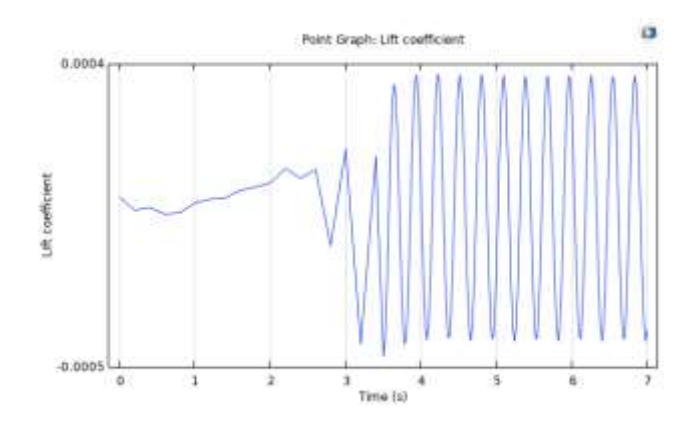


Fig. 3. 20 Lift coefficient, CL, as a function of time.

In Fig. (3.20.) shows at first, there are very slight oscillations in the lift coefficient, which indicates stable flow conditions. After about 3.5 seconds, however, periodic fluctuations start to show, indicating the beginning of vortex shedding and the formation of a von Kármán vortex street. Over time, these oscillations become stronger and more consistent, demonstrating how unsteady wake formation is influenced by both thermal boundary conditions and nanofluid characteristics. The lift coefficient's periodic nature indicates that the nanofluid's enhanced thermal conductivity encourages an earlier transition to unsteady flow. As the flow transitions from steady to unsteady behavior, the observed pattern demonstrates that the lift force acting on the cylinder becomes time-dependent.

Drag Coefficient Graph for Single Solid Cylinder

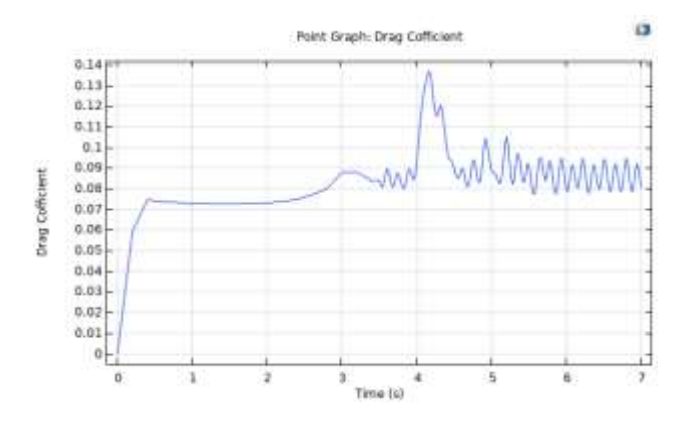


Fig. 3. 21 Drag coefficient, CD, as a function of time.

Fig. (3.21.) shows the drag coefficient rises dramatically before leveling off at about 0.075, signifying the emergence of steady-state laminar flow. However, the flow enters an unsteady regime at about 3.5 to 4 seconds, at which point noticeable variations in the drag coefficient start to appear. The start of vortex shedding coincides with this change. Periodic oscillations with small amplitudes take over after this, indicating a fully formed von Kármán vortex street behind the obstacle. The time to reach unsteady flow is somewhat shortened by the use of nanofluid, whose increased thermal conductivity encourages instability in the boundary layer earlier. Overall, the findings show that by altering flow separation and heat transfer at the solid boundary, thermal effects and the presence of nanoparticles affect drag characteristics.

Lift Coefficient Graph for Double Solid Cylinder

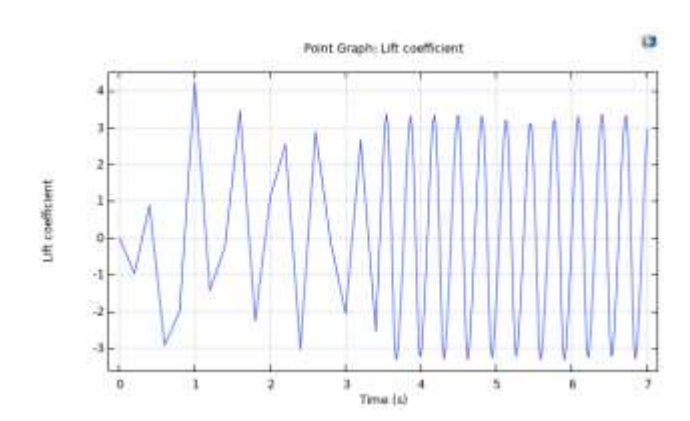


Fig. 3. 22 Lift coefficient, CL, as a function of time.

Fig. (3.22.) shows the flow is unstable in the early phases (0–2.5 s), which causes erratic fluctuations in the lift coefficient. The lift coefficient starts to periodically oscillate with increasing amplitude as time goes on (after about 3 seconds), signifying the beginning and stabilization of vortex shedding. The lift coefficient exhibits symmetric and repeating peaks and troughs, indicating that the von Kármán vortex street is fully formed by approximately 4 s. The development of the boundary layer is accelerated by the enhancement of thermal gradients and momentum diffusion close to the obstacle

surfaces caused by the presence of thermal boundary conditions and nanofluid. In contrast to a typical Newtonian fluid, this results in lift oscillations that are more noticeable and vortex formation that occurs earlier. Lift variations are further amplified by the complex wake dynamics created by the interaction between the two cylinders. Strong vortical structures that alternately emerge from each obstacle are confirmed by the alternating positive and negative peaks.

Drag Coefficient Graph for Double Solid Cylinder

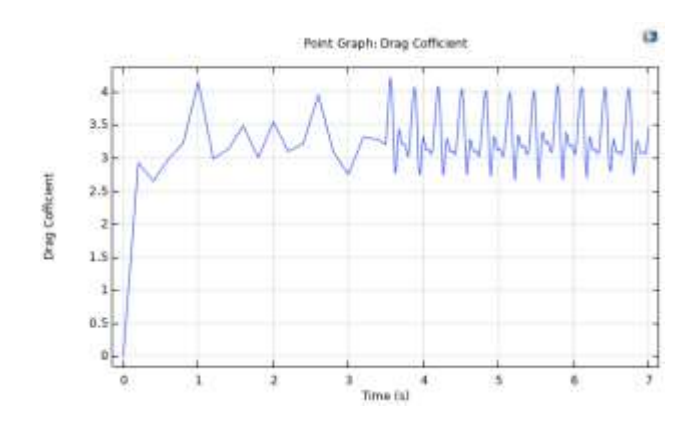


Fig. 3. 23 Drag coefficient, CD, as a function of time.

In Fig. (3.23.) shows due to transient flow development around both obstacles, the drag coefficient first shows a sharp rise from 0 to 1.5 seconds, followed by irregular fluctuations. As the nanofluid reacts to the applied thermal and flow boundary conditions, fluctuations reflect unstable wake interactions. these The system changes from chaotic to periodic behavior in 3–4 seconds. Four seconds later, the drag coefficient exhibits a distinct oscillatory pattern, signifying the onset of periodic vortex shedding. The two obstacles wake interference causes the drag values to fluctuate between a mean of about 3.2 and 3.4, with noticeable peaks rising above 4.0. Both the wake interaction between the obstacles and the increased thermal conductivity of the nanofluid are responsible for the higher drag levels when compared to single-obstacle scenarios. By improving momentum diffusion, the nanofluid thickens the boundary layer and increases drag forces. Furthermore, temperature gradients are further exacerbated by the thermal boundary conditions at the obstacle surfaces, which strengthen convective effects and increase drag variability.

Table. 3. 1 Mesh size and mesh properties for single solid obstacle.

		Recent work
Elements	Mesh 1	Mesh 2
Element Size	Normal	Extra Fine
Mesh Area	$0.8942m^2$	$0.8941m^2$

Table. 3. 2 Mesh size and mesh properties for double solid obstacles.

		Recent work
Elements	Mesh 1	Mesh 2
Element Size	Normal	Extra Fine
Mesh Area	$0.8865m^2$	$0.8863m^2$

3.4 Conclusion

Newtonian nanofluid flow through a 2D confined domain with single and double solid obstacles in circular cylinder was studied using CFD in this chapter. Heat transfer and fluid flow were simulated under thermal boundary conditions using the COMSOL Multiphysics platform. Thermal gradients at the inlet and solid wall boundaries were included in the study, which used a steady laminar flow model with a copper—water nanofluid.

The main findings of this chapter include:

The fluid's thermal conductivity and heat transfer throughout the domain were both improved by the addition of nanoparticles.

- ➤ Significant changes in velocity were caused by the flow contraction brought on by the solid cylinders; peak flow velocities, particularly in wake regions, reached up to 2.6–2.7 m/s.
- Lift and drag coefficient oscillations verified the periodic vortex shedding behind the obstacles, which was accompanied by the gradual formation of distinct von Kármán vortex structures.
- ➤ Surface temperature and pressure distributions displayed distinct gradients close to the obstacles, with double-obstacle cases showing pressure drops as low as -5.22×10³ Pa and maximum temperatures reaching 350 K.
- ➤ A second cylinder increased wake interactions, which led to more complicated recirculation zones and increased drag.
- ➤ With possible uses in energy, biomedical, and cooling system designs, this chapter shows that geometric obstruction, nanoparticle suspension, and thermal boundary conditions are important factors in altering the convective behavior of nanofluid flows inside channels.

Reference

- [1] Choi, S. U., & Eastman, J. A. (1995). Enhancing thermal conductivity of fluids with nanoparticles (No. ANL/MSD/CP-84938; CONF-951135-29). Argonne National Lab.(ANL), Argonne, IL (United States).
- [2] Yan, S. R., Toghraie, et al (2020). The rheological behavior of MWCNTs–ZnO/Water–Ethylene glycol hybrid non-Newtonian nanofluid by using of an experimental investigation. Journal of Materials Research and Technology, 9(4), 8401-8406.
- [3] Elelamy, A. F., Elgazery, N. S., & Ellahi, R. (2020). Blood flow of MHD non-Newtonian nanofluid with heat transfer and slip effects: Application of bacterial growth in heart valve. International Journal of Numerical Methods for Heat & Fluid Flow, 30(11), 4883-4908..
- [4] Hatami, M., Hatami, J., & Ganji, D. D. (2014). Computer simulation of MHD blood conveying gold nanoparticles as a third grade non-Newtonian nanofluid in a hollow porous vessel. Computer methods and programs in biomedicine, 113(2), 632-641.
- [5] Abdelsalam, S. I., & Bhatti, M. M. (2018). The study of non-Newtonian nanofluid with hall and ion slip effects on peristaltically induced motion in a non-uniform channel. RSC advances, 8(15), 7904-7915.
- [6] Zaman, A., & Khan, A. A. (2021). Time dependent non-Newtonian nano-fluid (blood) flow in w-shape stenosed channel; with curvature effects. Mathematics and Computers in Simulation, 181, 82-97.
- [7] Shojaie Chahregh, H., & Dinarvand, S. (2020). TiO2-Ag/blood hybrid nanofluid flow through an artery with applications of drug delivery and blood circulation in the respiratory system. International Journal of Numerical Methods for Heat & Fluid Flow, 30(11), 4775-4796.

- [8] Shahzadi, I., & Bilal, S. (2020). A significant role of permeability on blood flow for hybrid nanofluid through bifurcated stenosed artery: Drug delivery application. Computer methods and programs in biomedicine, 187, 105248.
- [9] Abdelsalam, S. I., Mekheimer, K. S., & Zaher, A. Z. (2020). Alterations in blood stream by electroosmotic forces of hybrid nanofluid through diseased artery: aneurysmal/stenosed segment. Chinese Journal of Physics, 67, 314-329.
- [10] Basha, H. T., Rajagopal, K., Ahammad, N. A., Sathish, S., & Gunakala, S. R. (2022). finite difference computation of Au-Cu/magneto-bio-hybrid nanofluid flow in an inclined uneven stenosis artery. Complexity, (1), 2078372.
- [11] Bhatti, M. M., & Abdelsalam, S. I. (2021). Bio-inspired peristaltic propulsion of hybrid nanofluid flow with Tantalum (Ta) and Gold (Au) nanoparticles under magnetic effects. Waves in Random and Complex Media, 1-26.
- [12] KOT, M. E., & ELMABOUD, Y. A. (2021). Hybrid nanofluid flows through a vertical diseased coronary artery with heat transfer. Journal of Mechanics in Medicine and Biology, 21(02), 2150012.
- [13] Manchi, R., & Ponalagusamy, R. (2022). Pulsatile flow of EMHD micropolar hybrid nanofluid in a porous bifurcated artery with an overlapping stenosis in the presence of body acceleration and joule heating. Brazilian Journal of Physics, 52(2), 52.
- [14] Bhatti, M. M. (2021). Biologically inspired intra-uterine nanofluid flow under the suspension of magnetized gold (Au) nanoparticles: applications in nanomedicine. Inventions, 6(2), 28.
- [15] Waqas, H., Farooq, U., Muhammad, T., & Manzoor, U. (2022). Importance of shape factor in Sisko nanofluid flow considering gold nanoparticles. Alexandria Engineering Journal, 61(5), 3665-3672.

- [16] Elnaqueb, T., Shah, N. A., & Mekheimer, K. S. (2019). Hemodynamic characteristics of gold nanoparticle blood flow through a tapered stenosed vessel with variable nanofluid viscosity. BioNanoScience, 9, 245-255.
- [17] Khan, U., Zaib, A., & Ishak, A. (2021). Magnetic field effect on Sisko fluid flow containing gold nanoparticles through a porous curved surface in the presence of radiation and partial slip. Mathematics, 9(9), 921.
- [18] Salvi, D., Boldor, D., Aita, G. M., & Sabliov, C. M. (2011). COMSOL Multiphysics model for continuous flow microwave heating of liquids. Journal of Food Engineering, 104(3), 422-429.
- [19] Sezgin, B., Caglayan, D. G., Devrim, Y., Steenberg, T., & Eroglu, I. (2016). Modeling and sensitivity analysis of high temperature PEM fuel cells by using Comsol Multiphysics. International Journal of Hydrogen Energy, 41(23), 10001-10009.
- [20] Adam, T., & Hashim, U. (2014). COMSOL multiphysics simulation in biomedical engineering. Advanced Materials Research, 832, 511-516.
- [21] Khan, I., Memon, A. A., Memon, M. A., Bhatti, K., Shaikh, G. M., Baleanu, D., & Alhussain, Z. A. (2020). Finite element least square technique for Newtonian fluid flow through a semicircular cylinder of recirculating region via COMSOL multiphysics. Journal of Mathematics, (1), 8869308.
- [22] Memon, A. A., Memon, M. A., Bhatti, K., Jacob, K., Sitthiwirattham, T., Promsakon, C., & Khan, I. (2022). Modelling and simulation of fluid flow through a circular cylinder with high Reynolds number: a COMSOL Multiphysics study. Journal of Mathematics, (1), 5282980.
- [23] Malikov, Z. M., Madaliev, M. E., Chernyshev, S. L., & Ionov, A. A. (2024). Validation of a two-fluid turbulence model in COMSOL Multiphysics for the problem of flow around aerodynamic profiles. Scientific Reports, 14(1), 2306.

- [24] Salem, S. F., & Tuchin, V. V. (2020). Numerical simulation of blood flow in a vessel by using comsol multiphysics® software. Annual Research & Review in Biology, 35(9), 76-82.
- [25] Wijayanti, W., Sasongko, M. N., & Kusumastuti, R. (2021). Modelling analysis of pyrolysis process with thermal effects by using Comsol Multiphysics. Case Studies in Thermal Engineering, 28, 101625.
- [26] Hussain, A., Hassan, A., Mdallal, Q. A., Ahmad, H., Sherif, E. S. M., Rehman, A., & Arshad, M. (2021). Comsolic solution of an elliptic cylindrical compressible fluid flow. Scientific reports, 11(1), 20030.
- [27] Ganie, A. H., Memon, A. A., Memon, M. A., Al-Bugami, A. M., Bhatti, K., & Khan, I. (2022). Numerical analysis of laminar flow and heat transfer through a rectangular channel containing perforated plate at different angles. Energy Reports, 8, 539-550.
- [28] Tarafder, M. S., & Mia, M. J. (2023, May). Comparative numerical simulation of laminar flow through pipe using Comsol Multiphysics and Openfoam. In Proceedings of the 13th International Conference on Marine Technology (MARTEC 2022).
- [29] Malikov, Z. M., Madaliev, M. E., Chernyshev, S. L., & Ionov, A. A. (2024). Validation of a two-fluid turbulence model in COMSOL Multiphysics for the problem of flow around aerodynamic profiles. Scientific Reports, 14(1), 2306.
- [30] Marín B, J. C., Amaya C, C. J., Ayala H, O. M., Ayala, O. F., & Ayala, M. (2023, October). Numerical study of the velocity profiles in an incompressible laminar flow with particles between two parallel plates. In ASME International Mechanical Engineering Congress and Exposition (Vol. 87660, p. V009T10A051). American Society of Mechanical Engineers.

- [31] Memon, A.A., Memon, M.A., Bhatti, K., Jacob, K., Sitthiwirattham, T., Promsakon, C., & Khan, I. (2022). Modelling and simulation of fluid flow through a circular cylinder with high Reynolds number: a COMSOL Multiphysics study. Wiley Online Library.
- [32] Cavanagh, K., & Wulandana, R. 2D flow past a confined circular cylinder with sinusoidal ridges. In Proceedings of the 2019 COMSOL Conference in Boston, Boston, MA, USA, (2019).
- [33] CFD Module User's Guide. Application Library path COMSOL Multiphysics/Fluid Dynamics/cylinder flow.
- [34] Rashidi, S., Bovand, M., & Abolfazli Esfahani, J. Application of magnetohydrodynamics for suppressing the fluctuations in the unsteady flow around two side-by-side circular obstacles. The European Physical.